APPENDIX A

Excerpts from PhD Thesis of Mohsen Banan

P-86

N91-22420

Chapter 4

Results

In this chapter the results of compositional and microstructural analyses of the solidified ingots are presented and discussed. The results are presented in two sections: 1) Solidification with axial vibration, and 2) Current-induced perturbations. The Vibration section consists of the microstructural and compositional analyses of the ingots solidified with and without vibration, the vibration-induced dynamic acceleration measurements, and the macroscopic growth rate measurements using an interface demarcation technique.

The Current-induced Perturbations section includes the results of solidification of an ingot with alternating current pulses, the current interface demarcation in an alloy of $In_{0.2}Ga_{0.8}Sb$, and *in – situ* temperature measurements in the charges of GaSb and $In_{0.2}Ga_{0.8}Sb$ during passage of electric current.

4.1 Solidification with Axial Vibration

Several ingots with a feed composition of $In_{0.2}Ga_{0.8}Sb$ were directionally solidified with and without axial vibration of the ampoule. Table 3.1 shows the experimental conditions for all the runs (this table is given in the Experimental chapter). An axial temperature gradient of 30-35 °C/cm (measured in using a K-type thermocouple in an empty ampoule) and an ampoule lowering rate of 8 mm/day or 21 mm/day were used in these solidification experiments. The actual axial temperature in the charge would be expected to be lower than in an empty ampoule. Such a difference arises primarily from the higher thermal con-

ductivity of a charge as compared to air. The temperature profile of the furnace used in our experiments was "thermally stable", meaning that the temperature increases upward into the furnace.

The freezing temperature of $In_{0.2}Ga_{0.8}Sb$ is about 690°C. Due to rejection of InSb, the freezing temperature decreases along the ingot. For good mixing of the melt and equilibrium at the freezing interface, the freezing temperature is predicted to vary from 690°C initially to 530° near the end of growth. Comparing the furnace temperature profile and the range of freezing temperature, the initial solidification front was expected to be near the heater and adiabatic zone boundary. The freezing temperature at the final stages of solidification would be in the vicinity of cooler and adiabatic zone.

4.1.1 Constitutional Supercooling in InSb-GaSb

For solidification of $In_{0.2}Ga_{0.8}Sb$ feed composition, a growth rate of 8 mm/day and an axial temperature gradient of 30-35°C/cm should avoid constitutional supercooling in the InSb-GaSb growth system. However, the temperature gradient in a charge is expected to be lower than 30-35°C/cm measured in an empty ampoule. At 21 mm/day growth rate, an axial temperature gradient of 30-35°C/cm or less(as in an ampoule with a charge under the same furnace setting) may not be large enough to avoid constitutional supercooling in the InSb-GaSb system.

To show the validity of the above statement, we may use equation A.8 describing the conditions for avoidance of constitutional supercooling given as (see Appendix A for more details):

$$G_{l_{critical}} \geq \frac{mVX_l}{D}\frac{C_c}{C_f}(k_i - 1) \tag{4.1}$$

Here m is the slope of the liquidus curve, k_i is the interfacial distribution coefficient, C_c and C_f are the total molar concentration of solute in the solid and liquid, respectively, X_l is the mole fraction of solute in the liquid at the interface, and V is the growth rate. C_c and C_f are calculated using the density and molecular weight data given in Appendix B and C. Fitting the liquidus curve for the phase diagram of InSb-GaSb we obtain:

$$T = 709.5 - 93.1X_l - 96.1X_l^2 \tag{4.2}$$

where X_l is the mole fraction of InSb in the liquid. The slope of the liquidus is determined as:

$$m = \frac{dT}{dX_l} = -93.1 - 192.2X_l \tag{4.3}$$

From the phase diagram, the equilibrium distribution coefficient k_o is determined as a function of liquidus composition as:

$$k_o = \frac{X_s}{X_l} = 0.12 + 0.721X_l - 2.37X_l^2 + 2.57X_l^3 \tag{4.4}$$

where X_s is the mole fraction of solute in the solid at the equilibrium interface. Assuming that equilibrium prevails at the interface, the interfacial distribution coefficient is the same as the equilibrium distribution coefficient, i.e. $k_i = k_o$.

Figure 4.1 shows plots of equation (4.1) for $G_{l_{critical}}$ versus X_l mole fraction of InSb in the liquid at the interface for growth rates of 8 mm/day and 21 mm/day and an assumed diffusion coefficient of 2×10^{-5} cm^2/s. The growth system is predicted to be stable for imposed temperature gradients above the curves and unstable for values below the curves for the given growth velocities. Interface breakdown is expected to appear as a cellular or dendritic structure resulting in axial and radial compositional fluctuations. The compositional variations arise from trapping of solute within the cellular structure or dendrites.

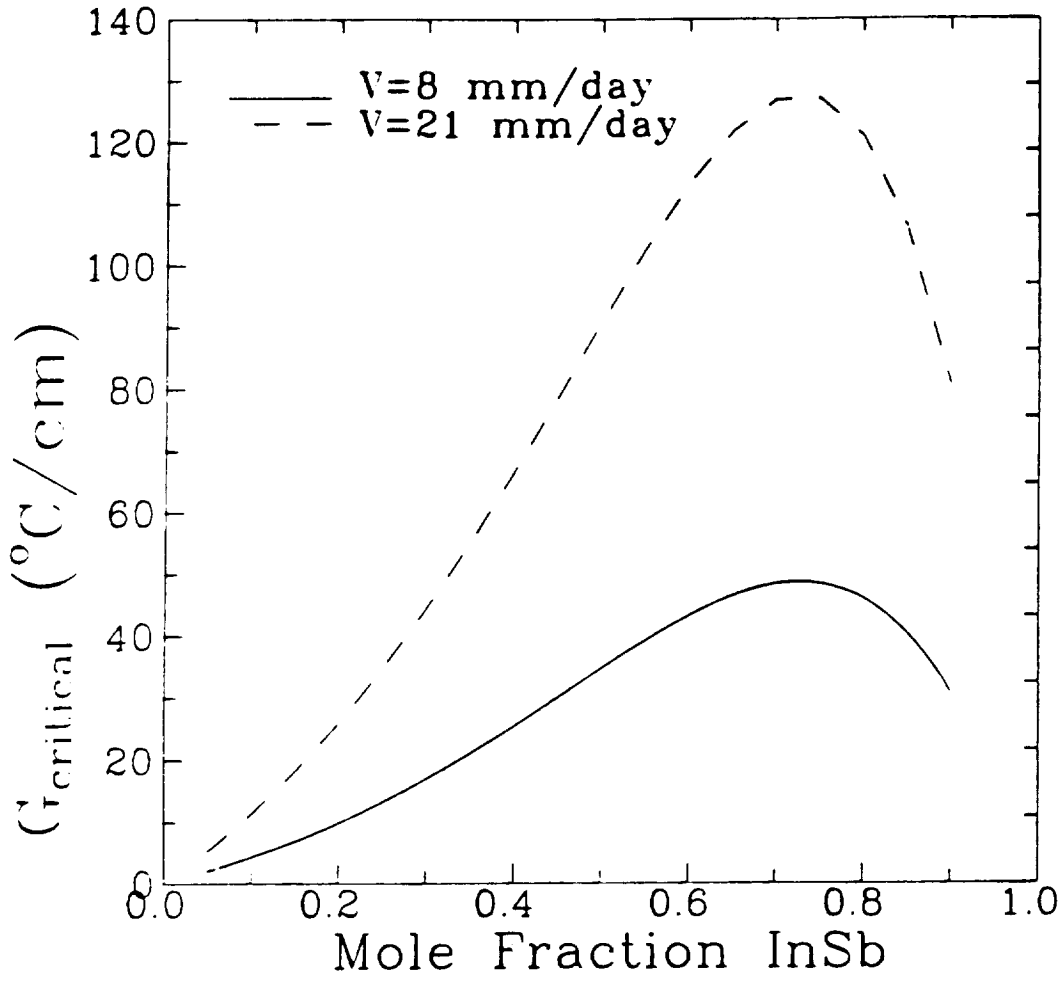

Figure 4.1: A plot of $G_{lcritical}$ in equation 4.1 versus mole fraction of InSb in the melt for InSb-GaSb system. Two growth rates were used: 8 mm/day and 21 mm/day. The system is predicted to be stable for an imposed temperature gradient above the curve and unstable for values below the curve for the given growth velocity.

4.1.2 Axial and Radial Compositions

The axial and radial composition profiles of the ingots were determined using energy dispersive spectrometry (EDS). The mole fraction of InSb was measured at 1 mm intervals along the longitudinal sections. The radial compositional profile of ingots was determined at 1 mm intervals across the samples taken from positions along the ingot. The experimental EDS analysis technique is described in detail in Chapter 3. The EDS analysis calculations, a compositional model for good mixing in the melt, calculation of the longitudinal concentration profile, and the error analysis of the EDS spectra data, are given in Appendix B.

Solidification at 8 mm/day Translation Rate

Figure 4.2 shows axial compositions versus longitudinal position of $In_xGa_{1-x}Sb$ ingots with feed composition of x_o=0.2. These ingots were directionally solidified at 8 mm/day ampoule translation rate and 30-35°C/cm axial temperature gradient (measured in an empty ampoule using a K-type thermocouple). The complete mixing theory curve was calculated using the formulations given in Appendix B. Within experimetal error the composition profiles all corresponded to good mixing in the melt for all ingots solidified, both with and without vibration.

The elevated indium composition in the first to freeze portion of the ingot was probably due to rapid freezing following nucleation from a supercooled melt. Similar initial compositional variations due to delayed nucleation were also observed in directionally solidified $Pb_xSn_{1-x}Te$ [84] and $In_xGa_{1-x}Sb$ [6] ingots.

Figures 4.3 and 4.4 show radial compositional profiles of ingots D1 (no vibration) and V5 (40Hz,0.1mm). The concentration was very uniform across the ingot. Near the last portion of the ingot to freeze, the compositional variation across the ingots increased. This radial segregation might have been due to the shape of the interface becoming more concave as compared to the intial sections of the ingot. Such changes in the liquid-solid interface shape were revealed by interface demarcation technique (details are given in the section on Liquid-Solid Interface Shape). A larger radial segregation is expected near the

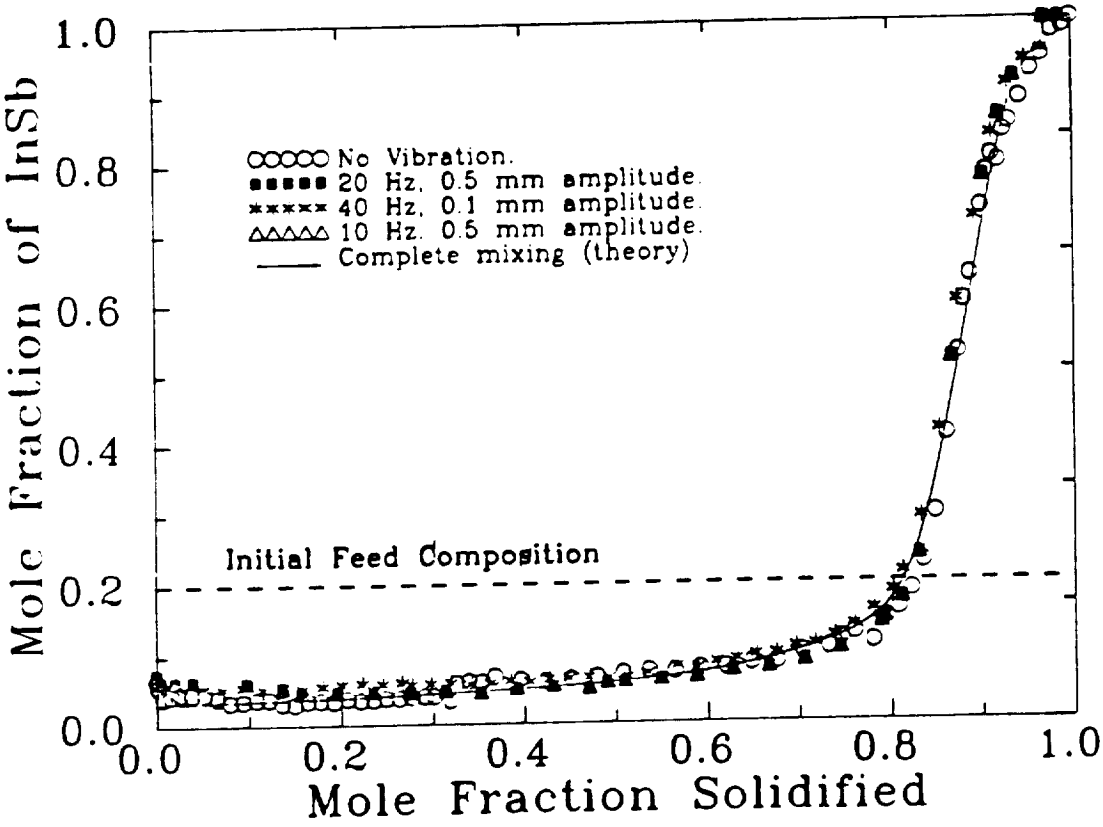

Figure 4.2: Axial composition profiles of ingots D1(no vibration), V1(10 Hz, 0.5 mm amplitude), V2(20 Hz, 0.5 mm amplitude), and V5(40 Hz and 0.1 mm amplitude). The mole fraction of InSb is given versus mole fraction solidified along the ingot. All experimental profiles correspond to good mixing in the melt.

end of the ingot because the concentration change more rapidly near the end of ingot and the interface becomes more concave. The wavy form of the radial composition at 90% fraction solidified of ingot D1 (no vibration) could have been due to enhanced mixing induced by Maragoni convection near the top of the free melt surface. In ingot V5 (40Hz,0.1mm), the radial composition variations near the end were large and asymmetrical. These variations could have been due to Maragoni convection at the free-melt surface, or oscillatory motion of the free melt surface by vibration.

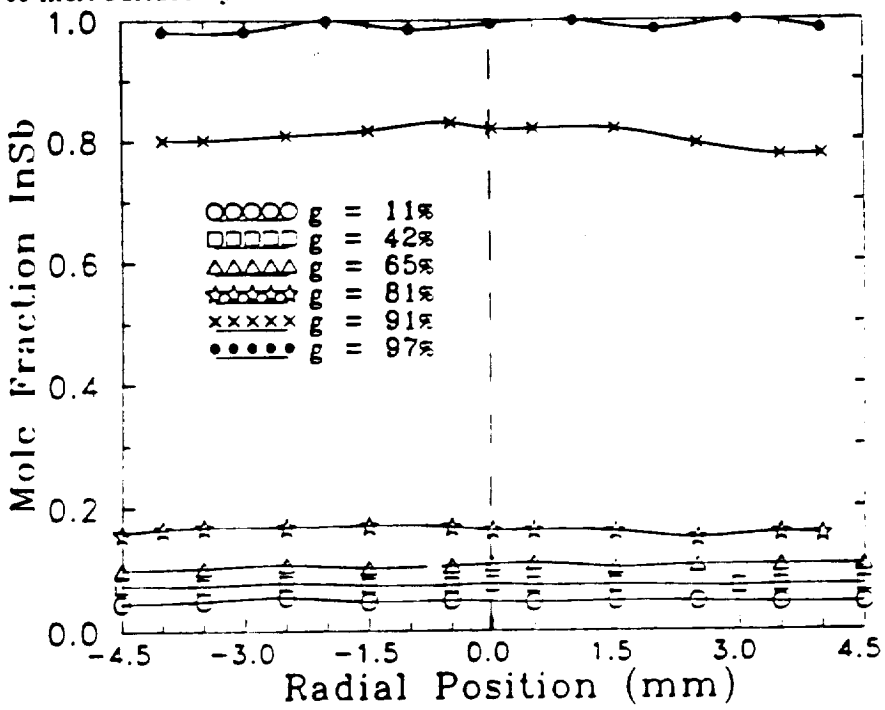

Figure 4.3: Radial composition profiles of ingot D1, which was solidified without vibration. Here g is the longitudinal mole fraction along the ingot.

The axial composition profiles of ingots V3 (20Hz, 1.0 mm amplitude), V4 (30 Hz, 0.5 mm amplitude), and V6 (100 Hz, 0.05 mm amplitude) are given in Figures 4.5, 4.7, and 4.8. The composition profiles corresponded to good mixing in the melt. The experimental curve is a little higher than the theoretically calculated curve. This difference could be due to EDS experimental errors and to deviation of the initial feed composition was from 20% mole InSb. Figure 4.6 shows the radial compositional profile of ingot V3 (20 Hz, 1.0 mm amplitude). The radial profile is uniform in composition. During solidification of ingots V3, V4, and V6 the furnace was shut off after partial solidification of the melt

in order to reveal the shape of the interface (results of interface shape are given in section 4.1.3).

The InSb-GaSb growth system is solutally stable, since the density of the rejected component, i.e. InSb, is more than the preferentially incorporated component, GaSb. All of these ingots were directionally solidified under thermally and solutally stable conditions. Vigorous convection is not anticipated under thermally and solutally stable conditions. The good mixing profile in the ingots solidified with vibration was due to enhanced mixing by vibration of the ampoule. However, the axial composition profile of ingot D1, solidified without vibration, corresponds to a profile for good mixing in the melt. The good mixing could have been due to convection induced by radial concentration and temperature gradients and/or molecular diffusion. Since the growth rate of 8 mm/day was very slow, there might have been sufficient time for diffusion to mix the rejected solute at the interface with the entire liquid (explained in the Discussion chapter).

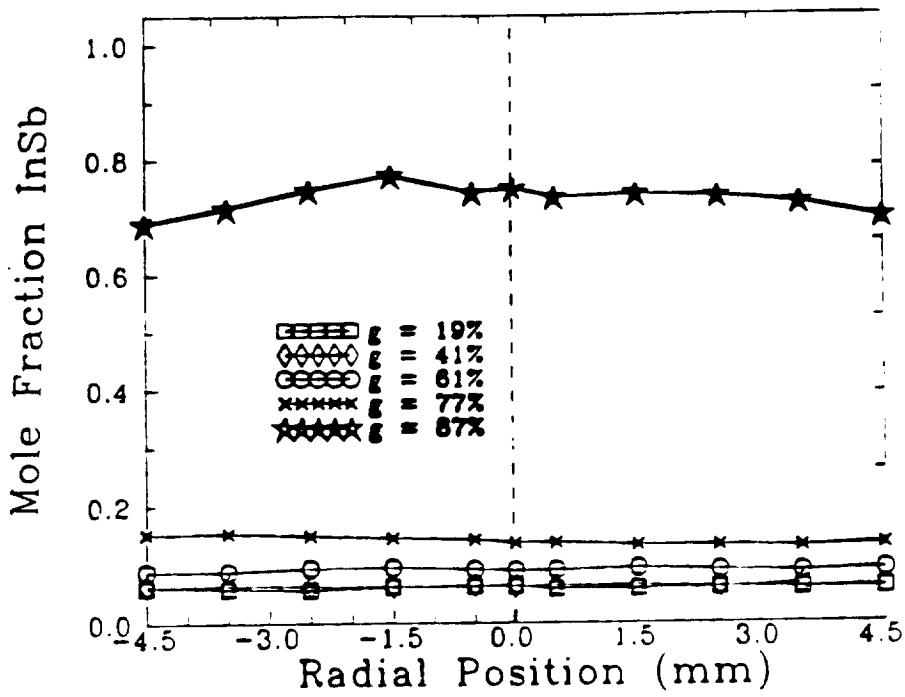

Figure 4.4: Cross-sectional composition profiles of ingot V5, solidified with vibration at 40 Hz and 0.1 mm amplitude. Here g is the longitudinal mole fraction along the ingot.

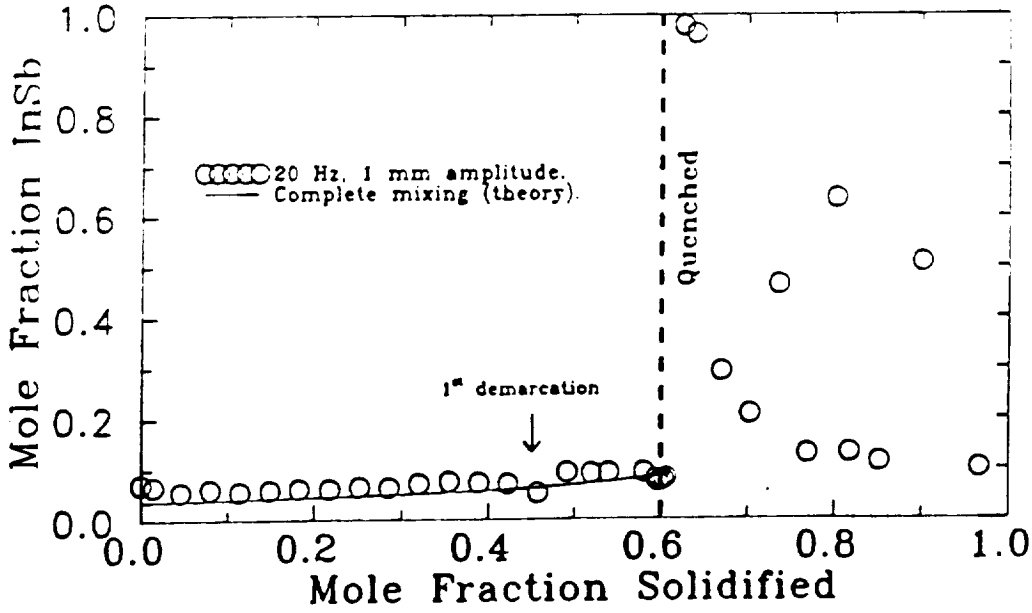

Figure 4.5: Axial composition profile of ingot V3 directionally solidified at 8 mm/day ampoule translation rate and axial vibration of 20 Hz frequency and 1.0 mm amplitude. The curve corresponds to good mixing in the melt.

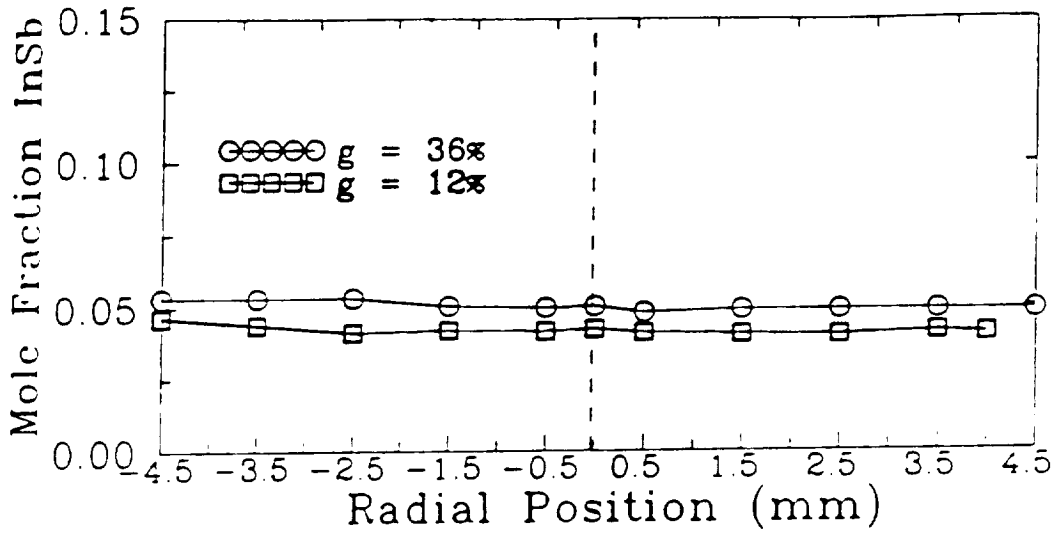

Figure 4.6: Radial composition profiles of ingot V3 which was solidified with vibration at 20 Hz and 1.0 mm amplitude. Here g is the longitudinal mole fraction along the ingot.

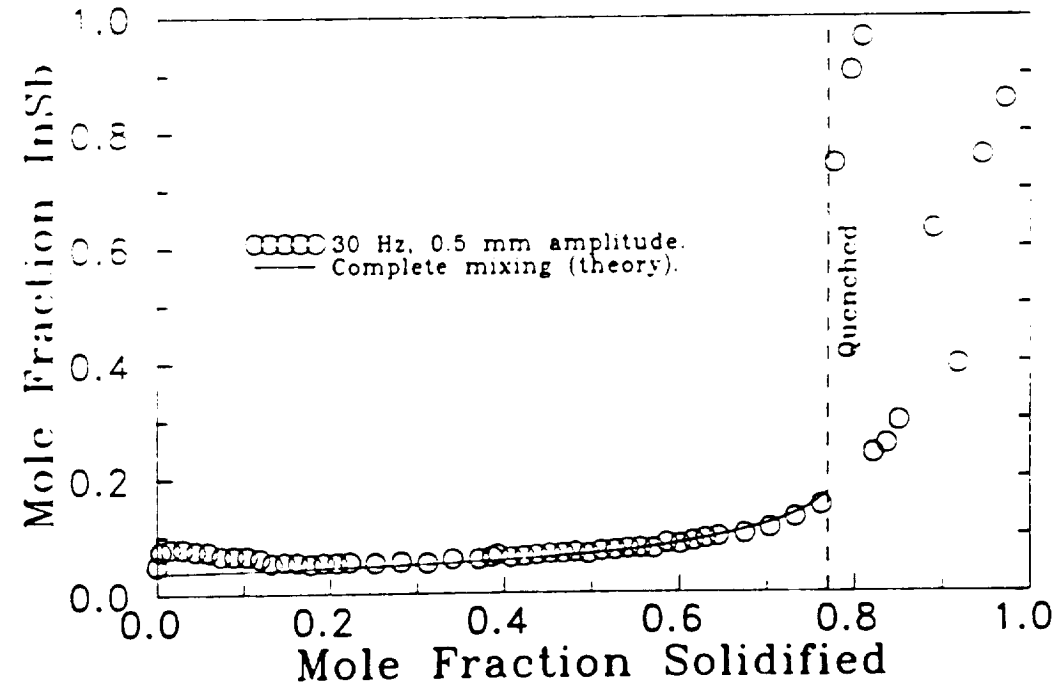

Figure 4.7: Axial composition profiles of ingot V4 directionally solidified at 8 mm/day and axial vibration of 30 Hz, 0.5 mm amplitude. The curve shows the composition profile predicted for complete mixing of the melt.

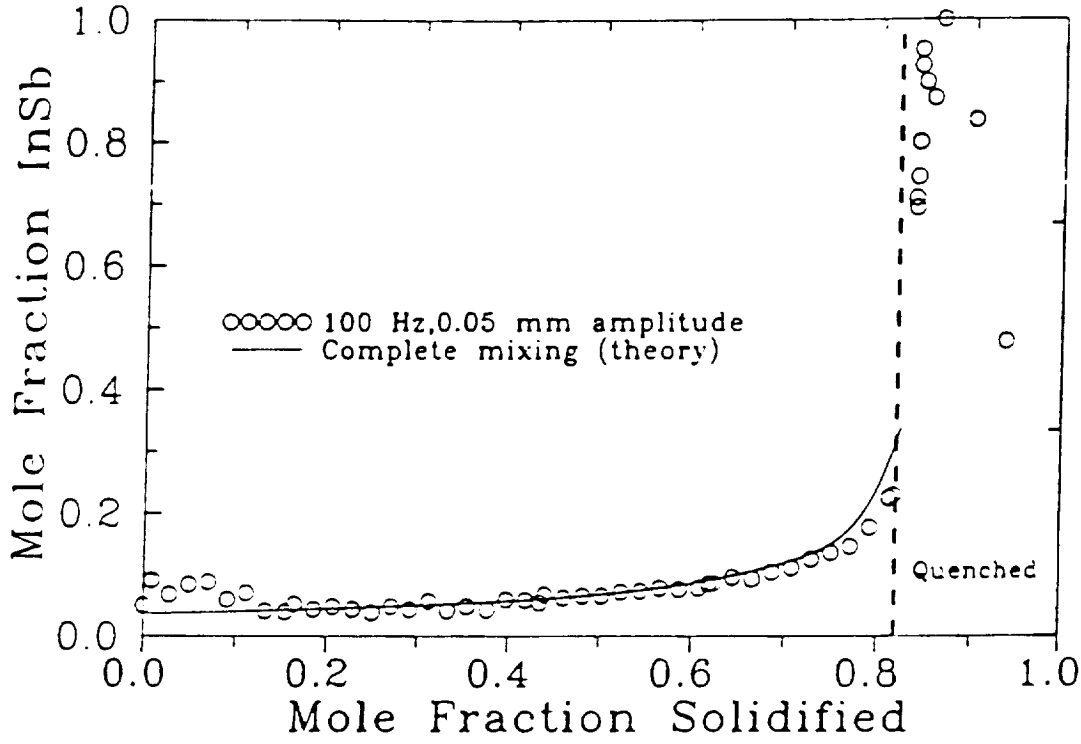

Figure 4.8: Axial composition profile of ingot V6 directionally solidified at 8 mm/day and axial vibration of 100 Hz frequency and 0.05 mm amplitude. The line is the predicted profile based on complete mixing of the melt.

Solidification at 21 mm/day Translation Rate

Three ingots with $In_{0.2}Ga_{0.8}Sb$ feed composition were solidified at 21 mm/day ampoule translation rate and 30-35 °C/cm axial temperature gradient (measured in an empty ampoule). One ingot was solidified without vibration, one with axial vibration at 20 Hz frequency and 0.5 mm amplitude, and one with 40 Hz frequency and 0.1 mm amplitude.

Figure 4.9 shows the axial composition profiles of ingots F1 (without vibration) and F2 (20 Hz,0.5 mm) solidified at 21 mm/day. The profiles correspond to good mixing in the melt. Compositional fluctuations were observed after 75 to 80% mole fraction of the ingots had solidified. The composition fluctuations might have been due to constitutional supercooling and morphological breakdown. An examination of the microstructure of both ingots showed a change in the microstructure from multi-grain with twins to a fine grain structure at near where the compositional fluctuations began. After 90% mole fraction had solidified, the axial composition again began following a good mixing pattern. This behavior occurred sooner in the ingot solidified with vibration compared to the one solidified with vibration. Figures 4.10 and 4.11 show the radial composition profiles of ingots F1 and F2.

Figure 4.1 (refer to the beginning of this chapter) shows the critical temperature gradient, given in equation 4.1, in the melt plotted versus the mole fraction of InSb in the liquid at the interface for 8 mm/day and 21 mm/day growth rates. This figure is used to demonstrate the conditions for avoidance of constitutional supercooling in InSb-GaSb for givrn growth rates. A detail of the constitutional supercooling formulation is given in Appendix A and at the beginning of this chapter. An imposed axial temperature gradient of 30-35°C/cm (measured in an empty ampoule) was used in our solidification runs. The axial temperature gradient in an ampoule with a charge is expected to be lower than in an empty ampoule.

For solidification runs at 8 mm/day, the temperature gradient of 30-35°C/cm (the actual temperature gradient measured in a charge is lower than 30-35°C/cm) is above the critical temperature gradient for the entire range of InSb composition in the liquid at the interface. This means that the interface should remain stable throughout solidification of the entire ingot. As mentioned in section 4.1 for ingots solidified at 8 mm/day, the

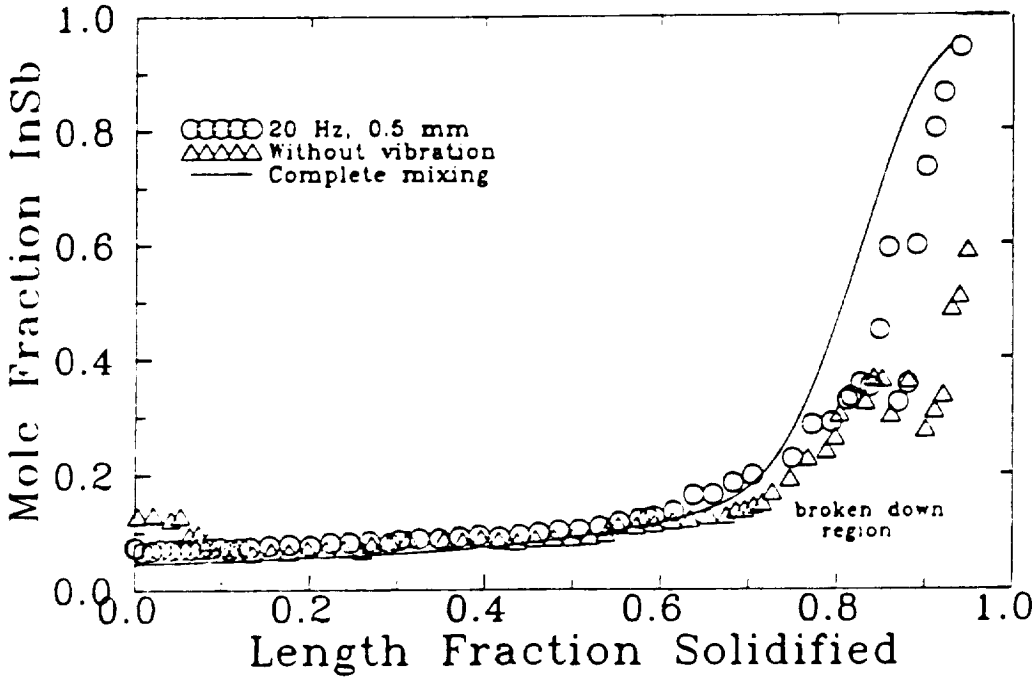

Figure 4.9: Axial composition profiles of $In_{0.2}Ga_{0.8}Sb$ feed composition ingots F1 (no vibration) and F2 (20 Hz,0.5 mm) directionally solidified at 21 mm/day. The continuous line is the theortical curve for good mixing in the melt.

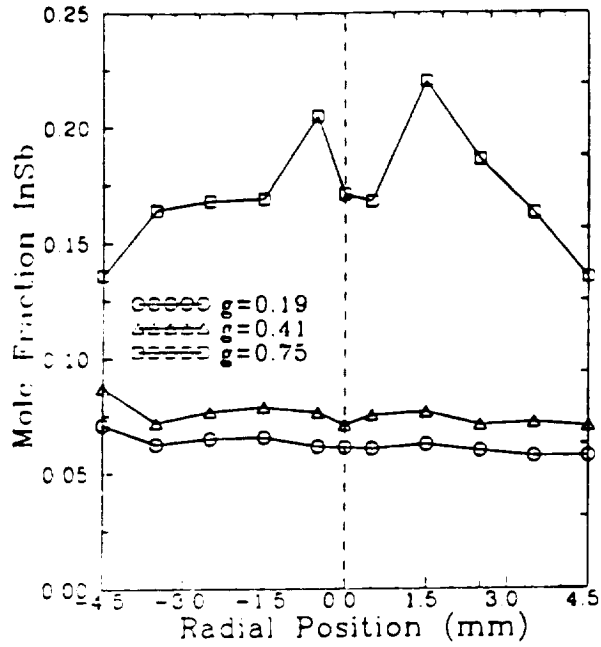

Figure 4.10: Radial composition profiles of ingots F1 solidified at 21 mm/day translation rate without vibration. Note g is the mole fraction solidified along the ingot.

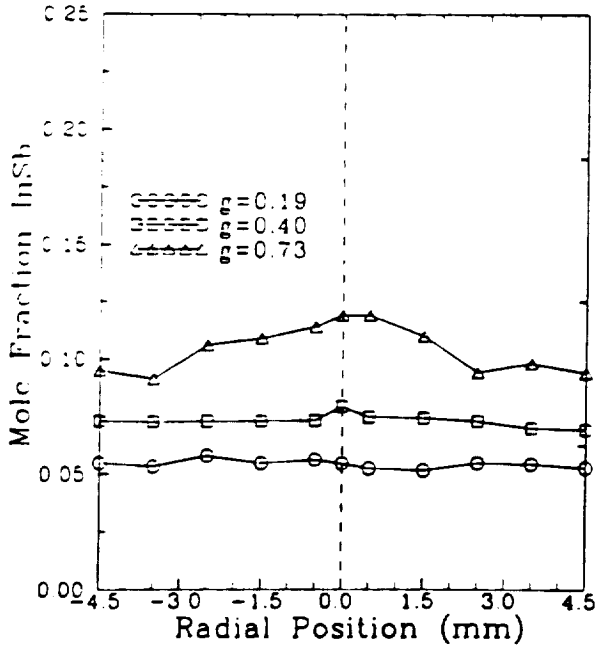

Figure 4.11: Radial composition profiles of ingots F2 solidified at 21 mm/day translation rate with vibration of 20 Hz and 0.5 mm amplitude. Note g is the mole fraction solidified along the ingot.

axial composition profiles corresponded to good mixing. No compositional fluctuations or other evidence of morphological breakdown were observed. In the ingots solidified at 21 mm/day, some compositional fluctuations were observed at and beyond 75-80% mole fraction solidified. The compositional fluctuations might have been due to morphological breakdown.

The location along the ingot that breakdown would take place could be related to the information given in Figure 4.1. The mole fraction InSb in the liquid at the interface can be determined at any given location along the ingot at the time solidification using the plots in Figure 4.12. Figure 4.12 shows the theoretical solute composition profile for the solid and liquid at the interface with equilibrium at the interface for good mixing of the melt for $In_{0.2}Ga_{0.8}Sb$ feed composition (calculation is given in Appendix B).The solute concentration increases in the melt ahead of interface. The mixing by free convection or vibration-induced convection might not be sufficient to reduce the solute build-up. Referring to Figure 4.12, the liquid composition at the interface at 80% mole fraction of ingot solidified was about 0.6 mole fraction InSb. The critical axial temperature gradient for 0.6 mole fraction of InSb in the liquid at 21 mm/day growth is about 100°C/cm. The actual growth rate with an ampoule lowering rate of 21 mm/day is less than 21 mm/day near the end of growth. The imposed axial temperature gradient during all our solidification runs was less than 30-35°C/cm , which is much lower than the critical temperature gradient of 100°C/cm. Consequently the interface should have broken down. Such morphological instability is expected to manifest itself as compositional fluctuations and fine grain structure, as observed in ingots F1 and F2.

The interface breakdown in ingots F1 and F2 extended for 0.15 mole fraction of the ingot solidified and then resumed a good mixing profile again. However, the composition profile near the end did not follow the good mixing profile for 0.20 mole fraction InSb, since the solute was trapped in the broken down region. This resulted in a change of composition in the melt and consequently in the solid near the end. Such a recovery from morphological breakdown could have been due to following; after the breakdown, the solute buildup ahead of the interface would be reduced since the solute is trapped in the broken-down regions.

The rate of growth also decreases due to interaction of the growth system with the furnace thermal fields (the growth rate measurements are given in section 4.3).

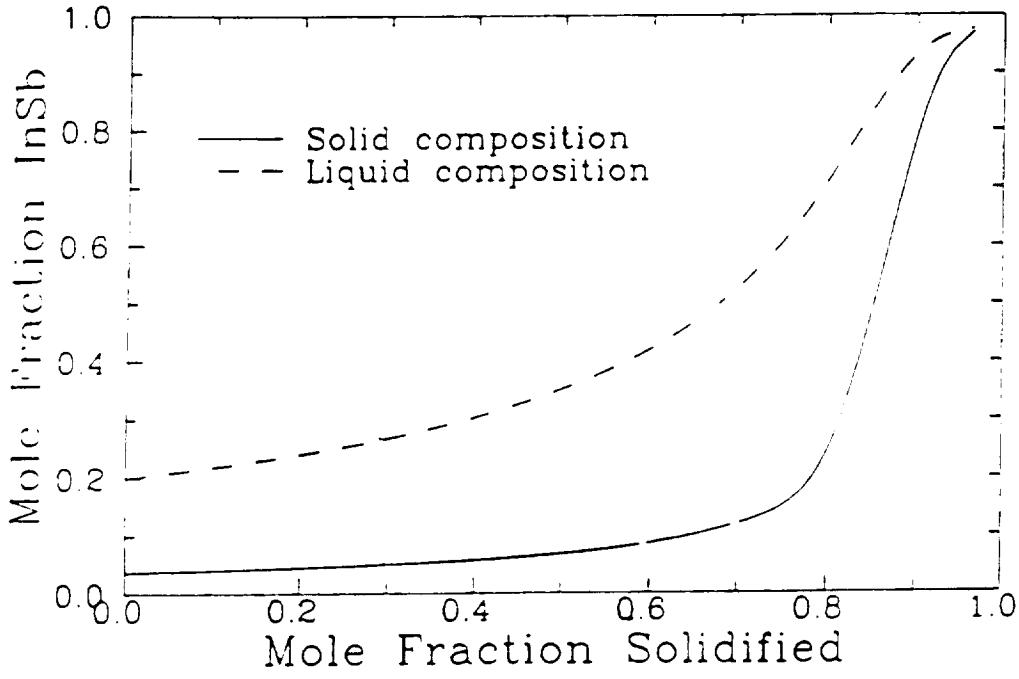

Figure 4.12: Calculated axial composition profile for an ingot with a feed composition of $In_{0.2}Ga_{0.8}Sb$ with equilibrium at the interface and good mixing in the melt. The continous curve is the calculated InSb composition in the solid at the interface. The dashed curve is the InSb composition in the liquid at the interface.

4.1.3 Liquid-Solid Interface Shape

Interface demarcations were generated in two ingots by lowering the heater temperature from 800°C to 770° and then abruptly translating the ampoule down by 1 mm. Afterward, the heater temperature was increased to 800°C again. The change of heater temperature would modify the thermal fields in the melt and charge, and cause fast freezing during the temperature lowering period. The ampoule was moved down by 1 mm to assure that the rapidly frozen demarcation would not backmelt.

The ingots were longitudinally sectioned, mechanically polished, and chemically etched in $1HF:1HNO_3:1H_2O$ for 30 sec to 2 minutes. A Longer etching time caused extensive cracking of the ingots. The demarcations appeared as discontinuities in the microstructure across the ingot. The demarcated lines had a sudden change of composition. The interface demarcations were not clear in the first half of the ingots, even after etching for 1 to 2 minutes. The demarcations were more pronounced at the second half, and especially near the end of the ingots. The less pronounced demarcations could be due to two reasons: the cooling period to induced fast freeze was not long enough and/or the preferential etching of second half as compared to first half of the ingots (the end portion had higher concentration of InSb compared to the first half of the ingots). At the first half of the ingots the shape of the interface was near-concave, with a radius of curvature less than 0.1 mm. The radius of curvature of the demarcations increased as solidification proceeded. In the last to freeze section of the ingots, the interface became more concave, with a radius of curvature of 1 mm. In these experiments no significant difference was observed in the demarcations' curvature in ingots solidified with or without vibration.

As mentioned earlier in the previous section ingots V3 (20 Hz, 1.0mm amplitude) and V6 (100 Hz, 0.05mm amplitude) were quenched after partial solidification. The shape of the interface in ingot V3 was convex, as shown in Figure 4.13. The first demarcation was made by lowering the heater temperature similar to the procedure mentioned above. The second demarcation was generated by quenching the remaining melt by shutting off the heater. The microstructure changed across the demarcation due to the discontinuity in growth rate. The first demarcation was very clear. The second demarcation was not

pronounced. The ingot cracked in the vicinity of the second demarcation during cutting. The EDS measutements showed the compositional variations across the demarcations. The corresponding axial composition profile is given in Figure 4.14. The compositions profile of the directionally solidified portion corresponded to good mixing in the melt. The interface shape was convex with 0.25 mm radius of curvature. A convex interface is desirable for better grain selection, since the grains tend to grow normal to the interface.

Figures 4.15 shows an interface demarcation generated by quenching the remaining melt during solidification of ingot V6. The ingot was chemically etched using $1HF:1HNO_3:1H_2O$ for 25 sec at room temperature to reveal the microstructure and interface demarcation. The interface was concave with a radius curvature of 0.3 mm. The interface was wavy and asymmetric. Figure 4.16 shows the axial composition profile in ingot V6. The composition suddenly changed at the demarcation location. The location of the interface demarcation along the ingot correspoded to freezing temperature of 600°C. The temperature of 600°C in our furnace was in the lower section of the adiabatic zone. It is expected that the interface shape would be near-concave in the boundary of adiabatic zone and the cooler.

Figure 4.13: Microstructure of ingot V3 translated at 8 mm/day with axial vibration of 20 Hz frequency and 1.0 mm amplitude. The interface demarcations were made by rapidly freezing the melt. The ingot was sandblasted to reveal the microstructure and the interface demarcations. The interface was convex with a radius of curvature of 0.25 mm. The ingot diameter was 9 mm. The growth direction was from left to right.

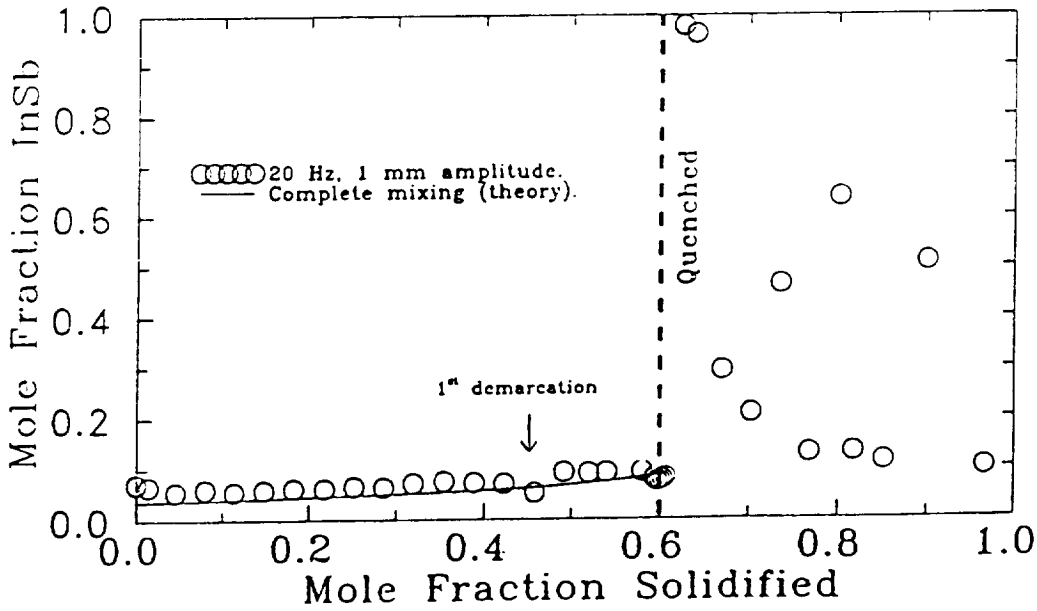

Figure 4.14: Axial composition profile of ingot V3.

Figure 4.15: Microstructure of last portion of ingot V6 to freeze with a translation rate of 8 mm/day and axial vibrations of 100 Hz frequency and 0.05 mm amplitude. The interface demarcations were made by rapidly freezing the melt. The ingot was chemically etched using $1HF{:}1HNO_3{:}1H_2O$ for 25 sec at room temperature to reveal the microstructure and interface demarcation. The interface was concave with a radius of curvature of 0.3 mm. The diameter of the ingot was 0.9 cm. The growth direction was from left to right.

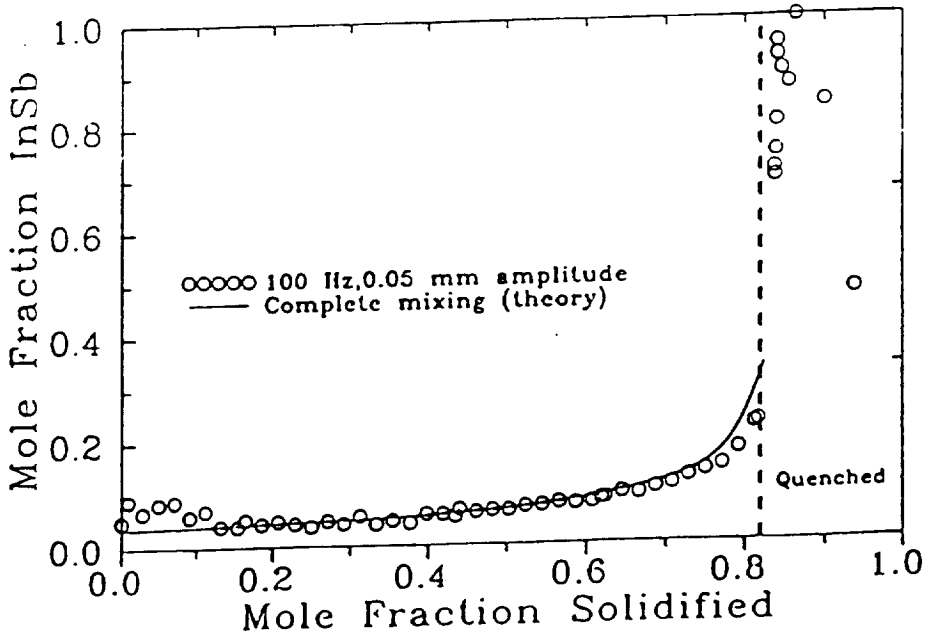

Figure 4.16: Axial composition profile of ingot V6.

4.1.4 Macroscopic Growth Rate

The macroscopic growth rate was determined for two ingots with $In_{0.2}Ga_{0.8}Sb$ feed composition, one without vibration and with vibration at 20 Hz frequency and 0.5 mm amplitude. The quenching interface demarcation technique was used. Both ingots were directionally solidified at 9.5 mm/day ampoule lowering rate.

In this technique the heater temperature was decreased from 800°C to 770°C within 10 minutes by lowering the voltage to the heater. When the heater temperature reached 770°C, the ampoule was abruptly moved downward by 1 mm. After the ampoule was moved down by 1 mm, the heater temperature was increased again to 800°C and maintained at that temperature. This procedure was undertaken every 24 hours during the entire solidification period of 15 to 16 days. After completion of a growth run, the ingot was removed from the ampoule. The ingot was sectioned axially and chemically polished using $1HF:1HNO_3:1H_2O$ for 60 sec at room temperature, to reveal the demarcations.

Figure 4.17 shows the measured distance between the above demarcations along the ingots. The measured distance versus time was fitted into a third degree polynomial. The macroscopic growth velocity along the ingot was calculated taking the derivative ofthe polynomial fit of the plots of distance versus time. A plot of macroscopic growth velocity versus length fraction solidified along the ingots is shown in Figure 4.18. The growth velocity was initially higher than the translation rate, possibly due to the end effects as predicted by Sukanek [65]. As mentioned earlier in section 4.2, the axial composition profile of all ingots directionally solidified with and without vibration corresponded to good mixing of the melt and equilibrium at the interface. As the growth proceeds, rejection of InSb lowers the freezing temperature (as given by the phase diagram), resulting in variation of the freezing temperature along the length of the ingot. The freezing temperature was initially about 690°C and gradually decreased to 530°C near the end of ingot. Consequently, solidification would never reach a steady-state condition.

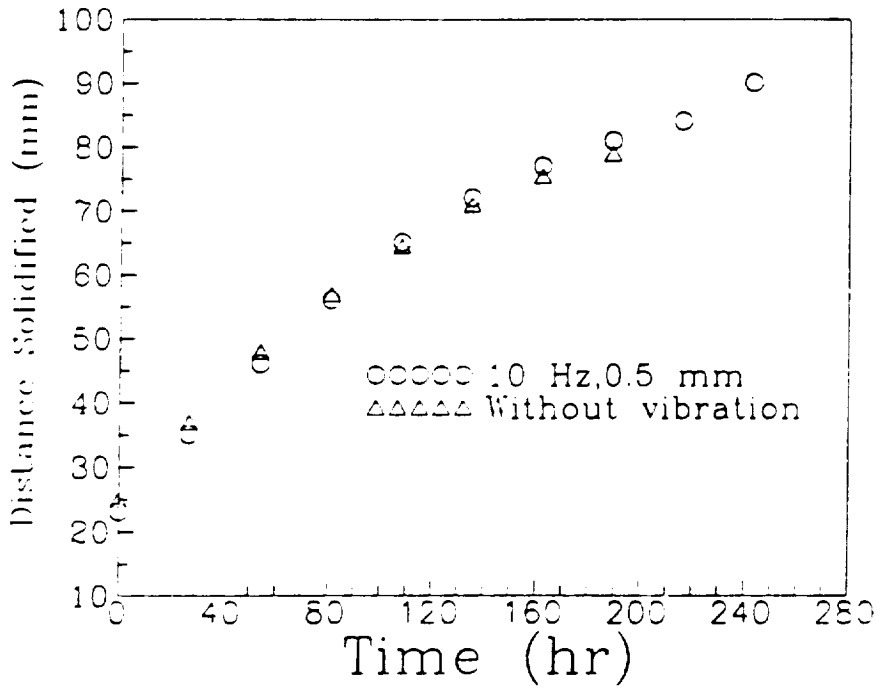

Figure 4.17: Position of interface demarcations versus time of generation. The circles and triangles represent the data for ingots solidified with vibration of 10 Hz and 0.5 mm amplitude and without vibration, respectively.

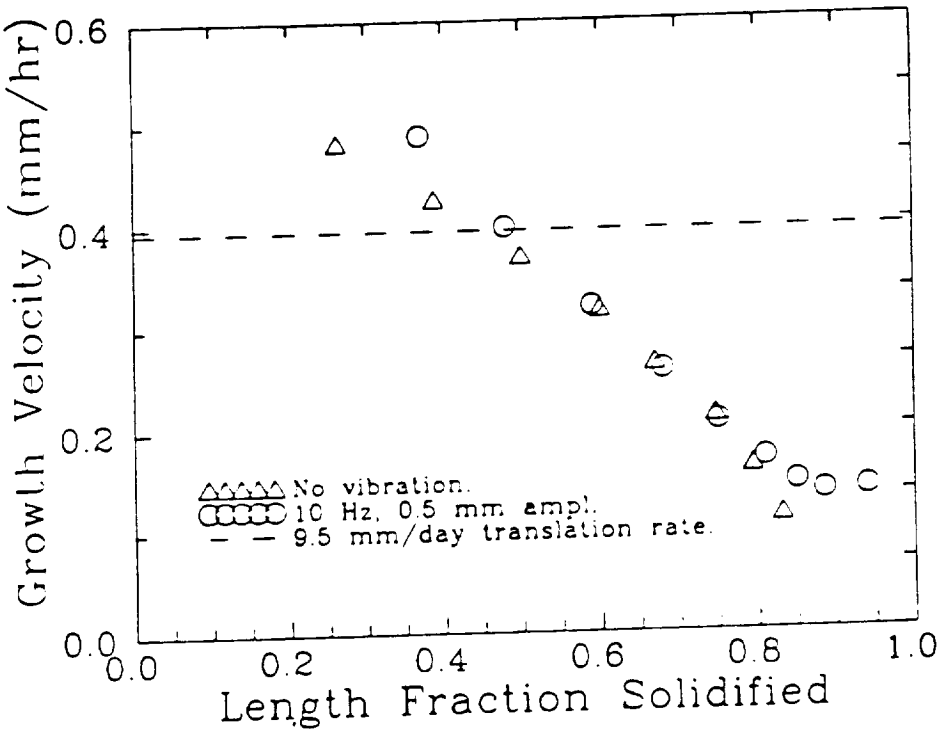

Figure 4.18: Macroscopic growth velocity versus length fraction solidified. Dashed line represents the ampoule translation rate of 9.5 mm/day. Note that the actual macroscopic growth velocity was always different from the translation rate throughout the entire growth period.

4.1.5 Vibration-induced Acceleration

Vibration of the ampoule resulted in modulation of acceleration in the direction of applied vibration. In our solidification experiments the growth ampoule was oscillated axially parallel to Earth's gravity. The dynamic acceleration induced by axial oscillation of the ampoule was measured using an accelerometer attached to the ampoule holder. The accelerometer's output signal was recorded at a sampling rate of 200 Hz using a data acquisition system and a Zenith 280 computer. Table 4.1 shows a summary of dynamic accelerations measured during axial vibration of the ampoule at different vibration paramters.

Figures 4.19 to 4.23 show the dynamic acceleration versus time for different vibrational conditions. Figure 4.19 shows acceleration fluctuations of $\pm 0.005 \times 9.81$ m/s^2 without any applied vibration. These fluctuations are caused by background noise in the laboratory. The vibration at 10 Hz frequency and 0.5 mm amplitude caused periodic acceleration variations of $\pm$ 0.1 $\times$ 9.81 m/s^2, as shown in Figure 4.20. A periodic variation of $\pm$ 0.2 $\times$ 9.81 m/s^2 was measured for vibration at 20 Hz frequency and 0.5 mm amplitude, as shown in Figure 4.21. Vibration at 40 Hz frequency and 0.1 mm amplitude resulted in $\pm$ 0.1 $\times$ 9.81 m/s^2 acceleration variations, as shown in Figure 4.22. Figure 4.23 shows the dynamic acceleration fluctuations of $\pm$ 0.05 $\times$ 9.81 m/s^2 measured during axial vibration at 100 Hz frequency and 0.05 mm amplitude.

The acceleration data were analyzed using the Power Spectrum option of TempleGraph software package (via Clarkson-NASA/Lewis computational facilities). The maximum g-variation was determined at its respective frequency for dynamic acceleration data of 20 Hz and 0.5 mm amplitude, 40 Hz and 0.1 mm amplitude, and 100 Hz and 0.05 mm amplitude, as shown in Figures 4.24, 4.25, and 4.26, respectively.

Table 4.1: Dynamic acceleration measured using an accelerometer at different vibration conditions. The acceleration varied periodically. Similar vibration parameters were used in the solidification experiments.

Ingot	Vibration Parameters (Hz),(mm)	Dynamic Acceleration (g=9.81 m/s^2)
V1	10.0.5	±0.09g
V2	20.0.5	±0.18g
V3	20.1.0	±0.23
V4	30.0.5	±0.25
V5	40.0.1	±0.10g
V6	100.0.05	±0.05g

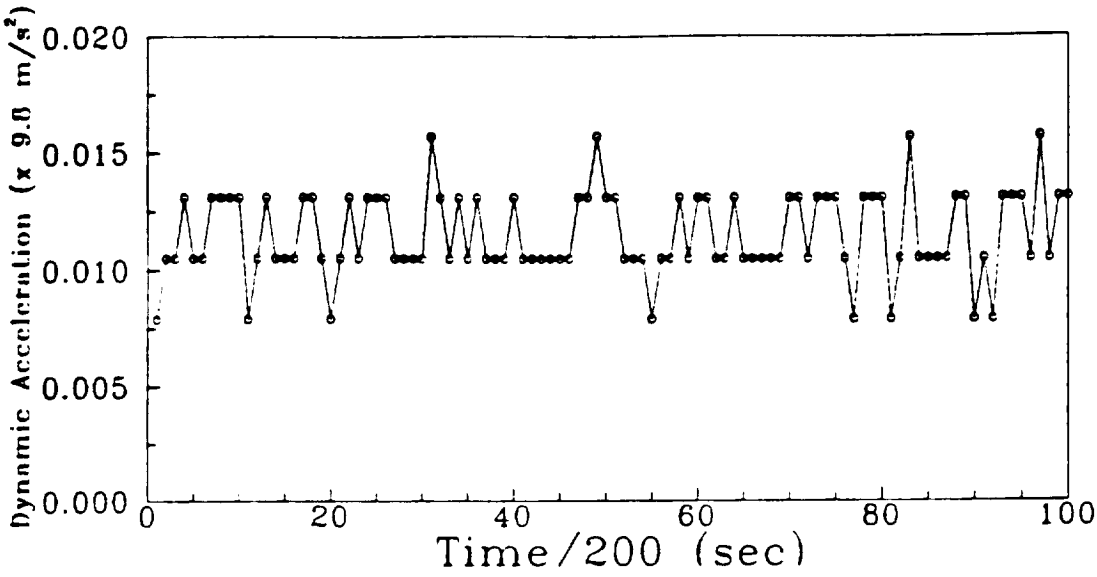

Figure 4.19: Plot of dynamic acceleration versus time without application of axial vibration. The measured fluctuations were due to background noise in the laboratory. The acceleration was measured using an accelerometer.

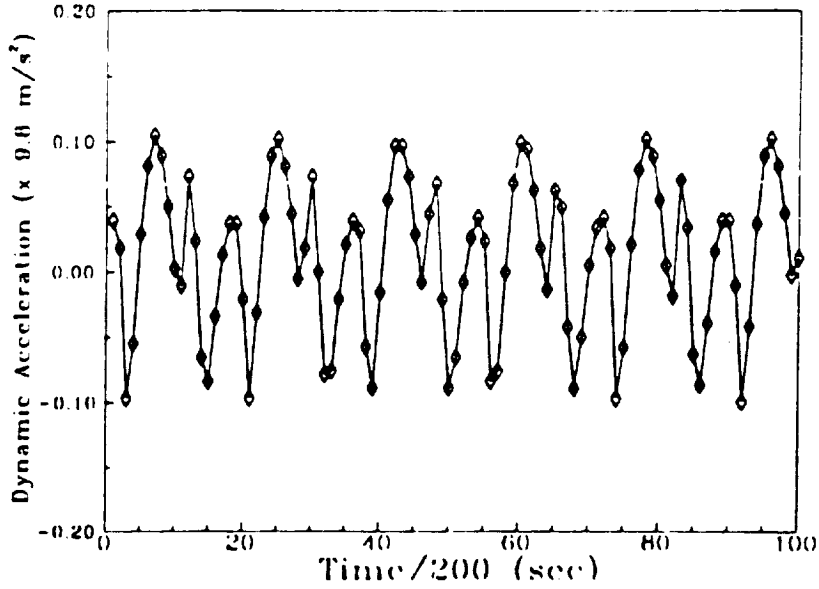

Figure 4.20: Plot of dynamic acceleration versus time with axial vibration at 10 Hz frequency and 0.5 mm amplitude. The acceleration was measured using an accelerometer.

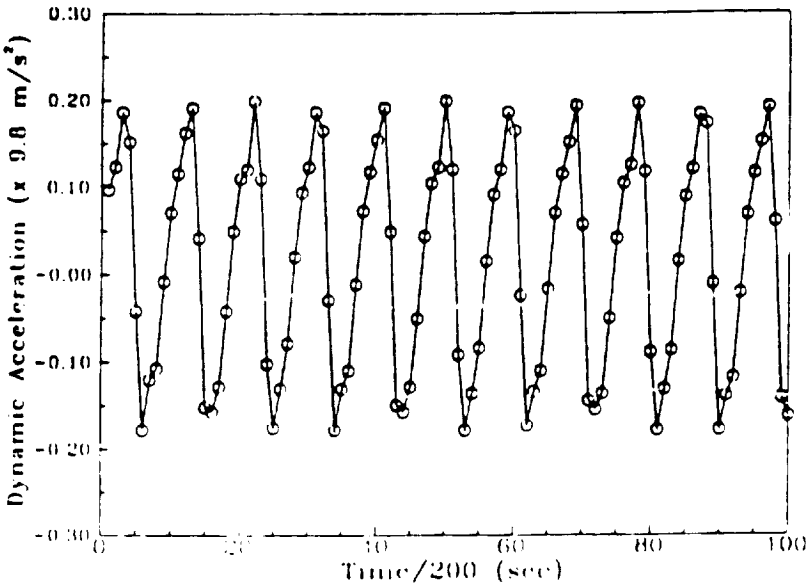

Figure 4.21: Plot of dynamic acceleration versus time with axial vibration at 20 Hz frequency and 0.5 mm amplitude. The acceleration was measured using an accelerometer.

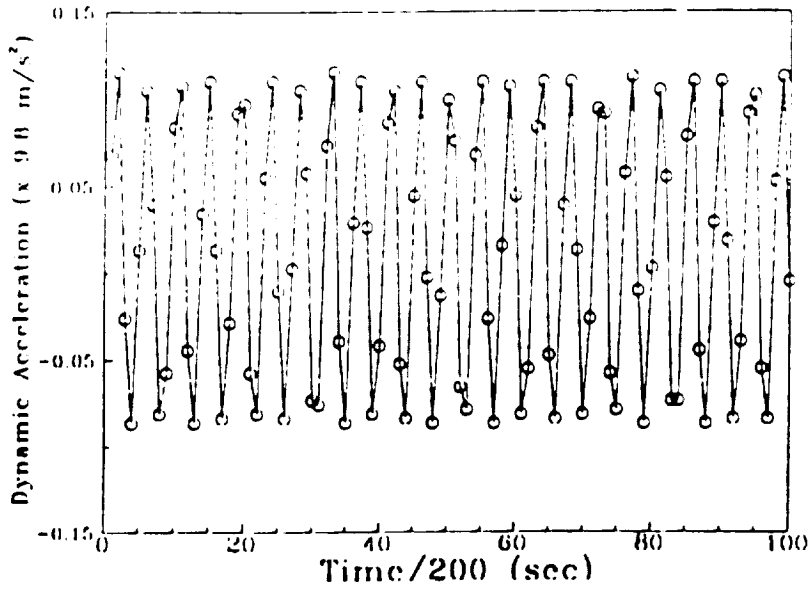

Figure 4.22: Plot of dynamic acceleration versus time with axial vibration at 40 Hz frequency and 0.1 mm amplitude. The acceleration was measured using an accelerometer.

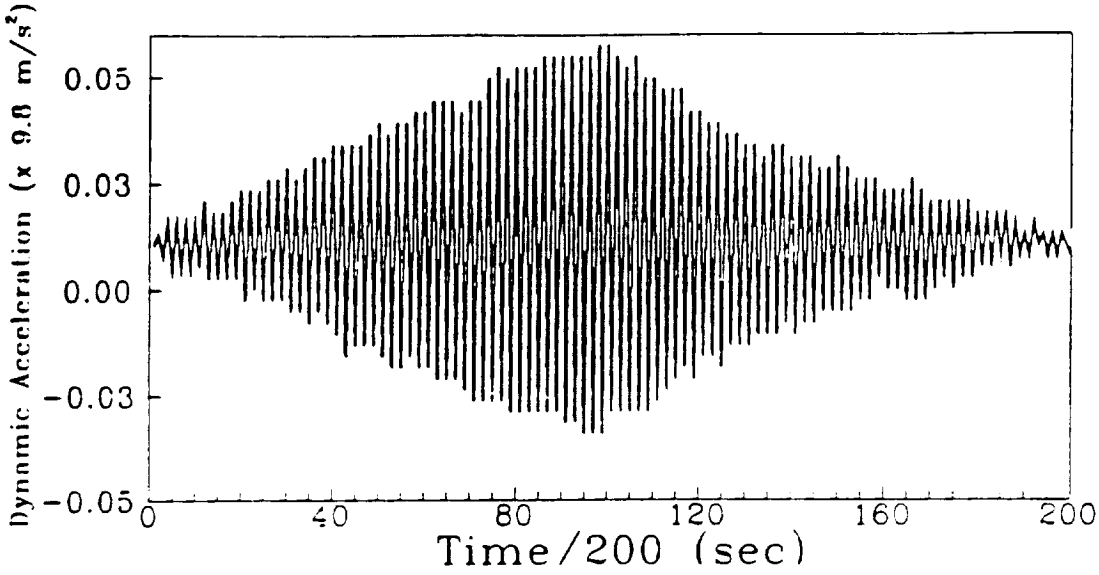

Figure 4.23: Plots of dynamic acceleration versus time with axial vibration at 100 Hz frequency and 0.05 mm amplitude. The acceleration was measured using an accelerometer.

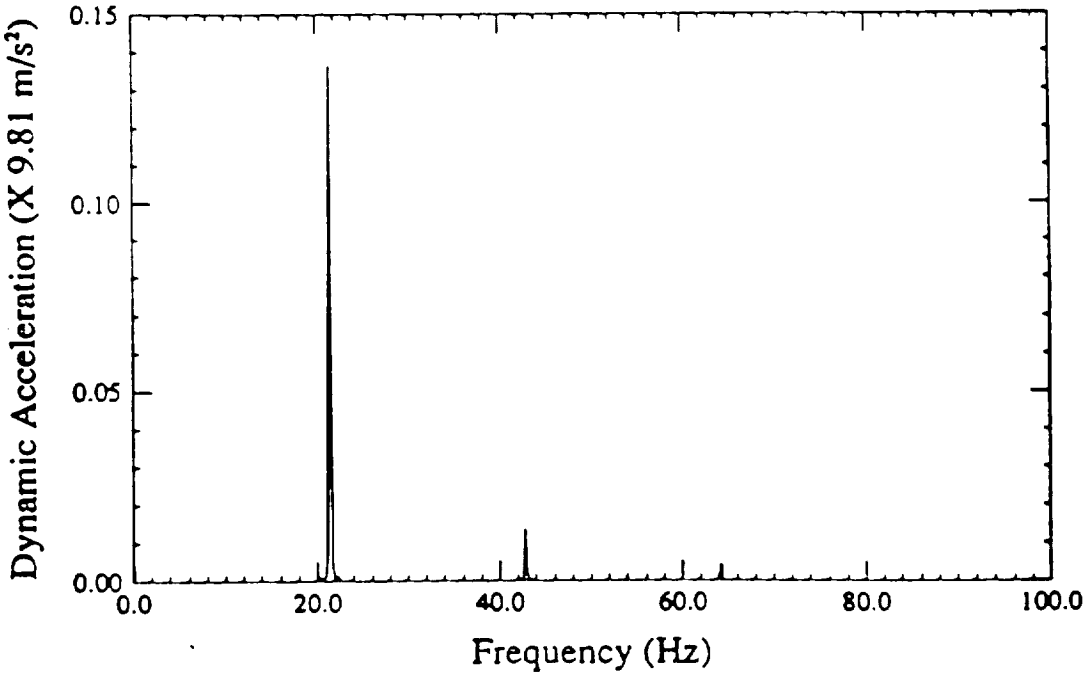

Figure 4.24: Power spectrum of dynamic acceleration at 20 Hz frequency and 0.5 mm amplitude vibration.

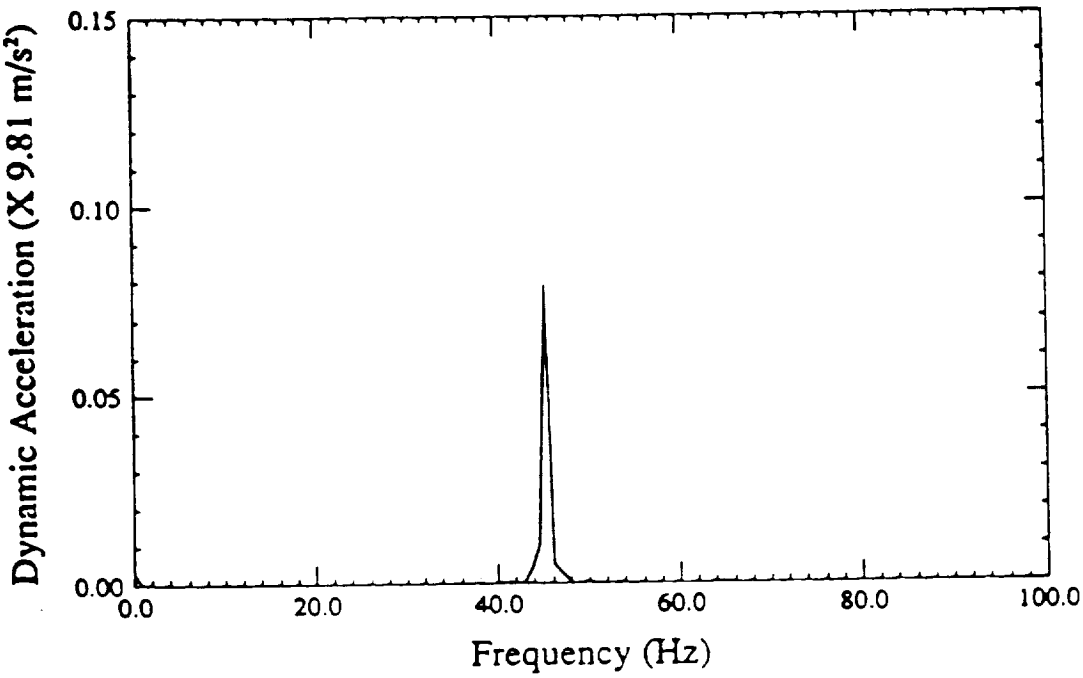

Figure 4.25: Power spectrum of dynamic acceleration at 40 Hz frequency and 0.1 mm amplitude vibration.

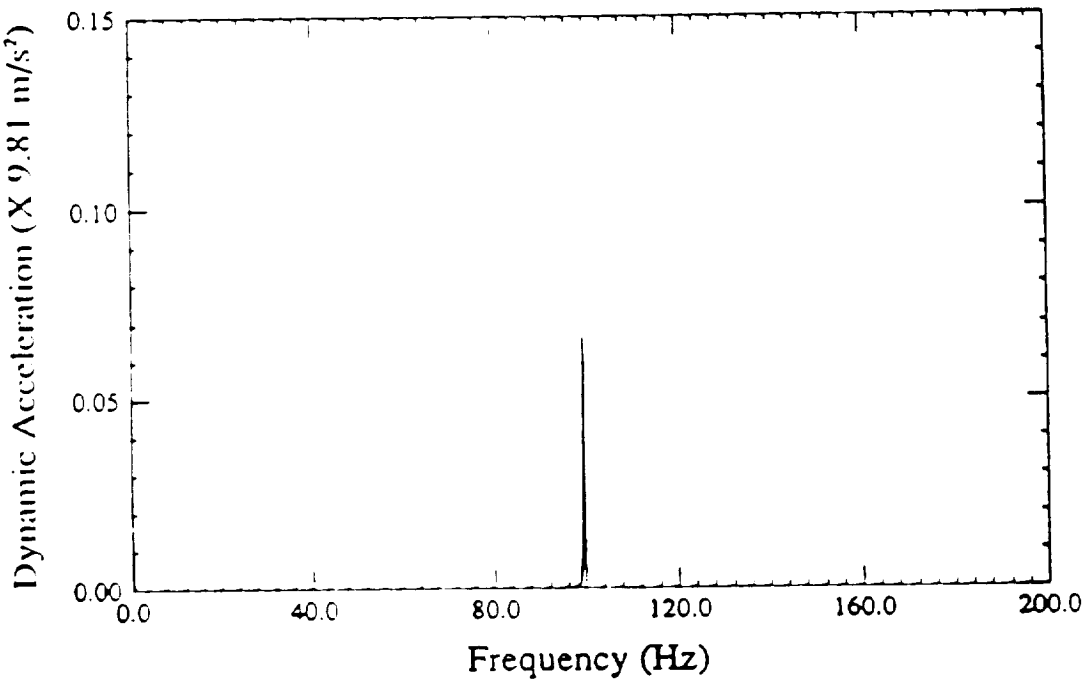

Figure 4.26: Power spectrum of dynamic acceleration at 100 Hz frequency and 0.05 mm amplitude vibration.

4.1.6 Microstructural Analysis

In this work, the entire ingot was sectioned longitudinally, as shown in Figure 4.27, for compositional and microstructural analyses. The compositional analysis was performed using a mechanically polished sample. For microstructural analysis, the longitudinal cross sections of ingots were mechanically polished and chemically etched to reveal the microstructure (details are given in Chapter 3).

Large number of voids (bubbles) were observed on the surface of the ingots, as shown in Figure 4.28. The number of bubbles was higher on the first half of the ingots as compared to the remaining portion. There was no correlation between the applied vibration and the number of bubbles on the surface of the ingots.

The microstructure of ingots was examined using optical microscopy at 200X magnification and scanning electron microscopy at 200X or higher. All ingots were polycrystalline. The microstructure consisted of many straight and curved boundaries. Etching of curved boundaries yielded a triangular groove. The straight boundaries appeared as rectangular-shape grooves. Figures 4.29 and 4.30 show scanning electron microscopy micrographs of the curved and straight boundaries after chemically etching of the sample in $HF:HNO_3:H_2O$ solution for 25 sec at room temperature. Figure 4.31 shows a scanning electron microscopy micrographs of a straight boundary at 1000X magnification. The rough surfaces are possibly due to preferential etching of regions with different orientation.

Figure 4.32 shows the microstructure of ingot D1 solidified without vibration. The boundaries were revealed by chemical etching the sample in $1HF : 1HNO_3 : 1H_2O$ solution
for 45 sec at room temperature. A large number of small grains was observed in the first to freeze section of ingot D1. This ingot consisted of a large number of curved and straight boundaries, with scattered small grains throughout the ingot.

Figure 4.33 shows a photograph of the microstructure of the longitudinal section of ingot V1 solidified with axial vibration of 10 Hz and 0.5 mm amplitude. The boundaries were revealed by chemically etching the sample in $1HF:1HNO_3:1H_2O$ solution for 45 sec at room temperature. Fewer small grains was observed in the first to freeze section

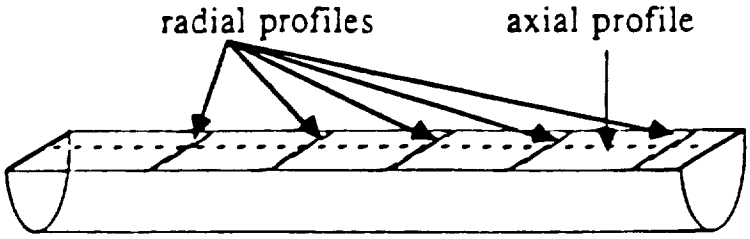

Figure 4.27: Schematic diagram of a longitudinally sectioned ingot used for compositional and microstructural analyses.

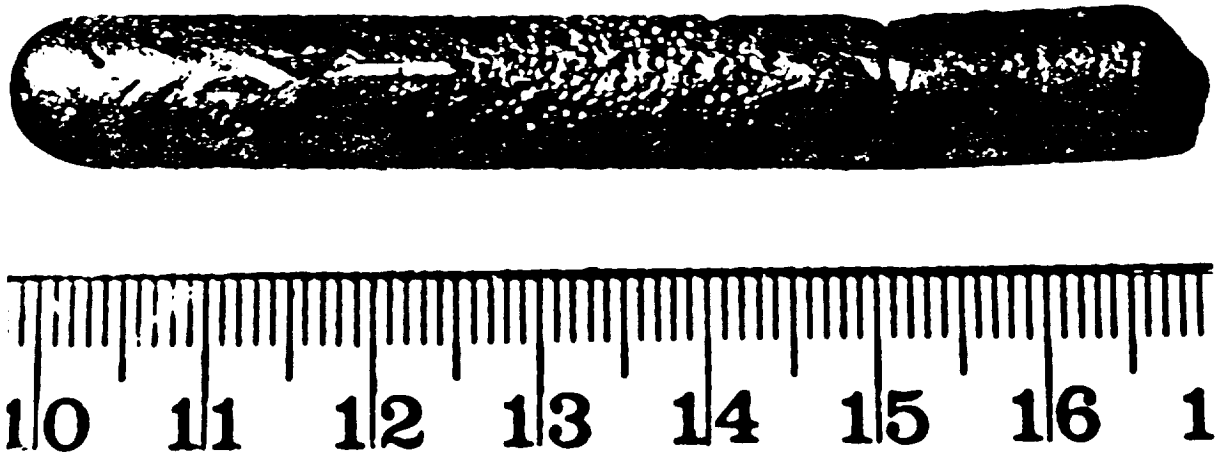

Figure 4.28: Sandblasted $In_xGa_{1-x}Sb$ ingot which was solidified with vibration at 20 Hz frequency and 0.5 mm amplitude. Bubbles were present on the surface of the ingot. Growth direction was from left to right.

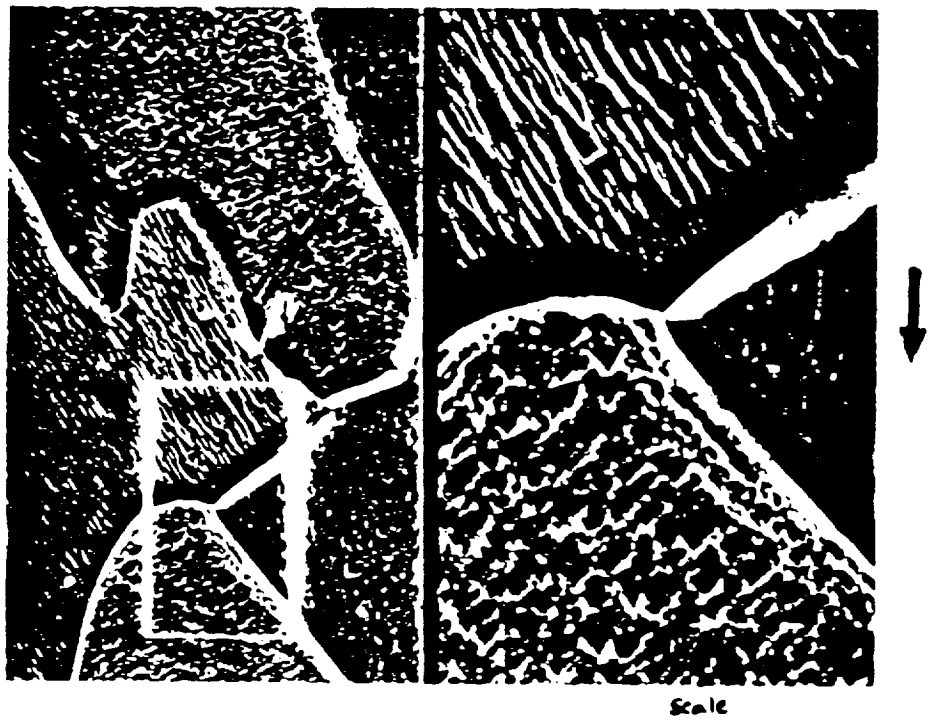

Figure 4.29: Scanning electron micrograph of curved boundaries on a longitudinal section of $In_{0.2}Ga_{0.8}Sb$ ingot V6. The boundaries were revealed by chemically etching the sample in $1HF:1HNO_3:1H_2O$ solution for 25 sec at room temperature. The magnifications are 300x and 900x for the pictures on the left and on the right, respectively. The picture on the right is an enlargement of the area enclosed in the box in the picture on the left. The scale bar is 10 microns and 3.3 microns for the 300X and 900X magnifications, respectively. The large arrow to the right indicates the growth direction.

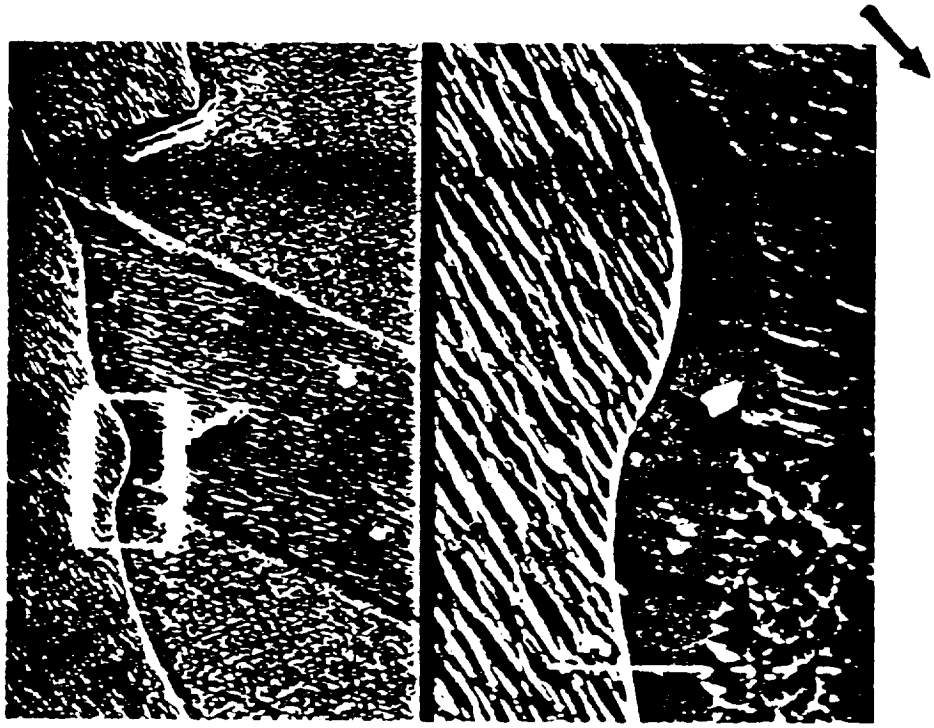

Figure 4.30: Scanning electron micrograph of curved and straight boundaries on a longitudinal section of $In_{0.2}Ga_{0.8}Sb$ ingot V6. The boundaries were revealed by chemically etching in $1HF:1HNO_3:1H_2O$ solution for 25 sec at room temperature. The magnifications are 200X and 1000X for the pictures to the left and to the right, respectively. The picture on the right is a 5 times enlargement of the boxed area in the picture on the left. The longest bar in the bottom of the picture is 100 and 20 microns for the 200X and 1000X magnifications, respectively. The large arrow indicates the growth direction.

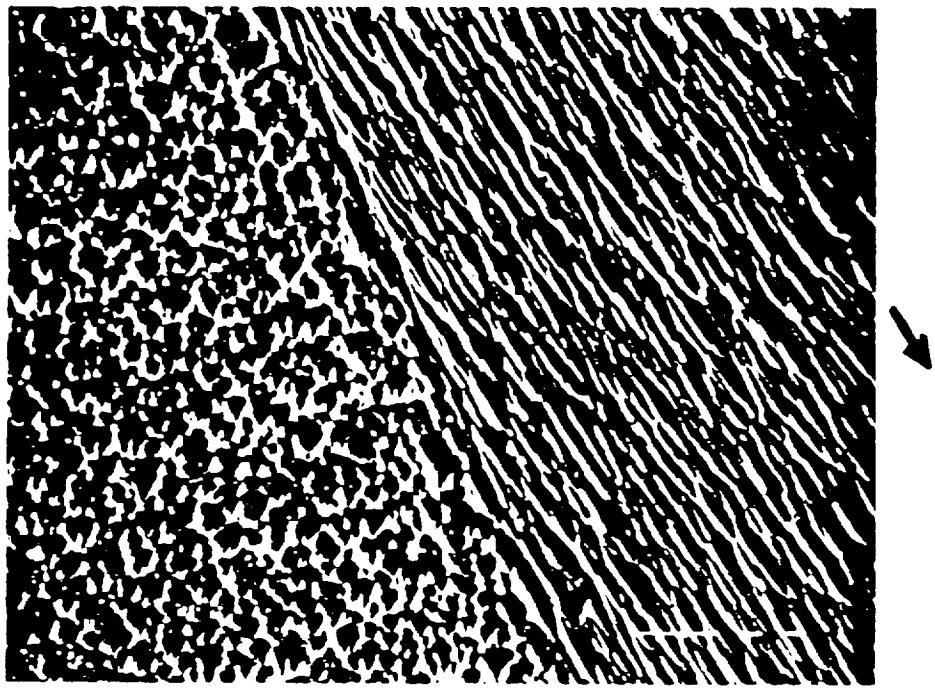

Figure 4.31: Scanning electron micrograph of a straight boundary on a longitudinal section of $In_{0.2}Ga_{0.8}Sb$ ingot V2. The surface was etched in $1HF:1HNO_3:1H_2O$ for 25 sec at room temperature. The magnification is 1000X. The longest bar at the bottom of the picture is 10 microns. The arrow indicates the growth direction.

Figure 4.32: Photograph of the microstructure of a longitudinal section of ingot D1, which was solidified at 8 mm/day translation rate without vibration. The boundaries were revealed by chemically etching the sample in $HF:HNO_3:H_2O$ solution for 45 sec at room temperature. The samples were cast in a resin mold for polishing. The width of the ingot is 0.9 cm. The growth direction was from left to right.

of ingot V1 as compared to ingot D1. Interestingly, growth of large grains was initiated from the first to freeze section of ingot V1. This ingot consisted of three grains initially and two grains near the end. A large number of twins initiated from the ampoule wall and grew inward. No small grain was observed in ingot V1.

Figure 4.34 shows a photograph of the microstructure of a longitudinal section of ingot V2, which was solidified with axial vibration of 20 Hz and 0.5 mm amplitude. Ingot V2 consisted of many small grains in the first to freeze section. Large twinned grains were observed after 4 to 5 mm from the first to freeze section of ingot V2. The twins were mostly initiated from the ampoule wall and grew inward until reached to a curved boundary. In the second half of ingot V2, there were only two grains, but heavily twinned. The twins in the second half were parallel to the growth direction.

Figure 4.35 shows a photograph of the microstructure of a longitudinal section of ingot V6, which was solidified at 8 mm/day with axial vibration of 100 Hz and 0.05 mm amplitude. In the first to freeze section of ingot V6, a large number of fine grains was present. The microstructure mostly consisted of grains in the first half of the ingot with only a few twins. In the second half of the ingot, the number of grains was reduced to three with several twins. The last portion of this ingot was quenched to reveal the liquid-solid interface. The interface shape was near concave with a wavy configuration. The wavy shape might have been due to oscillatory perturbations caused by vibration.

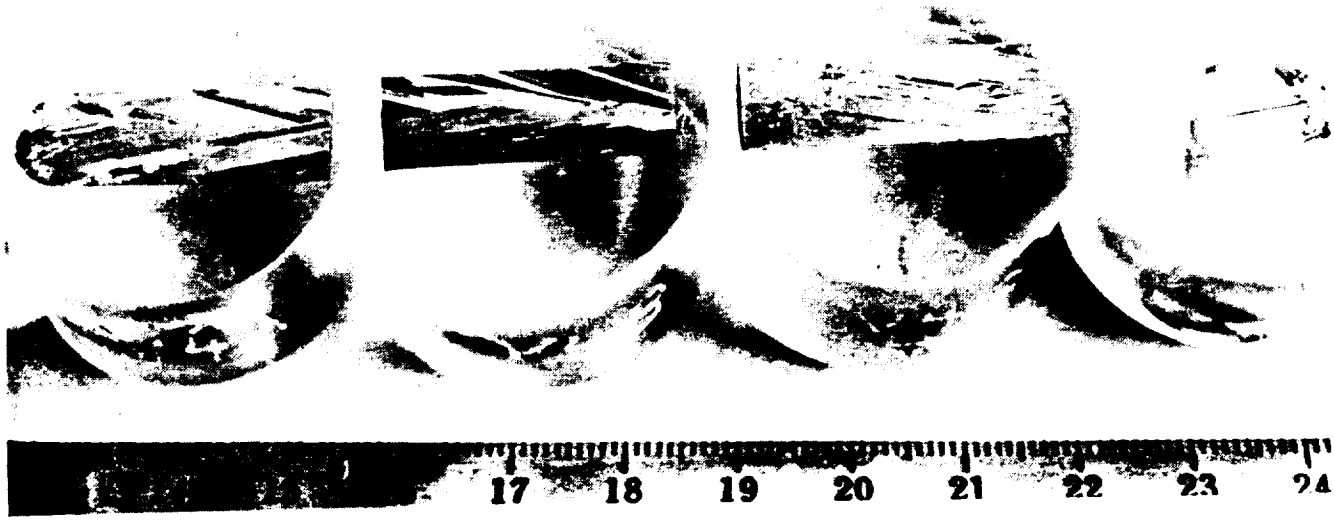

Figure 4.33: Photograph of the microstructure of a longitudinal section of ingot V1 solidified with axial vibration of 10 Hz and 0.5 mm amplitude. The boundaries were revealed by chemically etching the sample in $1HF:1HNO_3:1H_2O$ solution for 45 sec at room temperature. The samples were cast in a resin mold for polishing. The width of the ingot is 0.9 cm. The growth direction was from left to right.

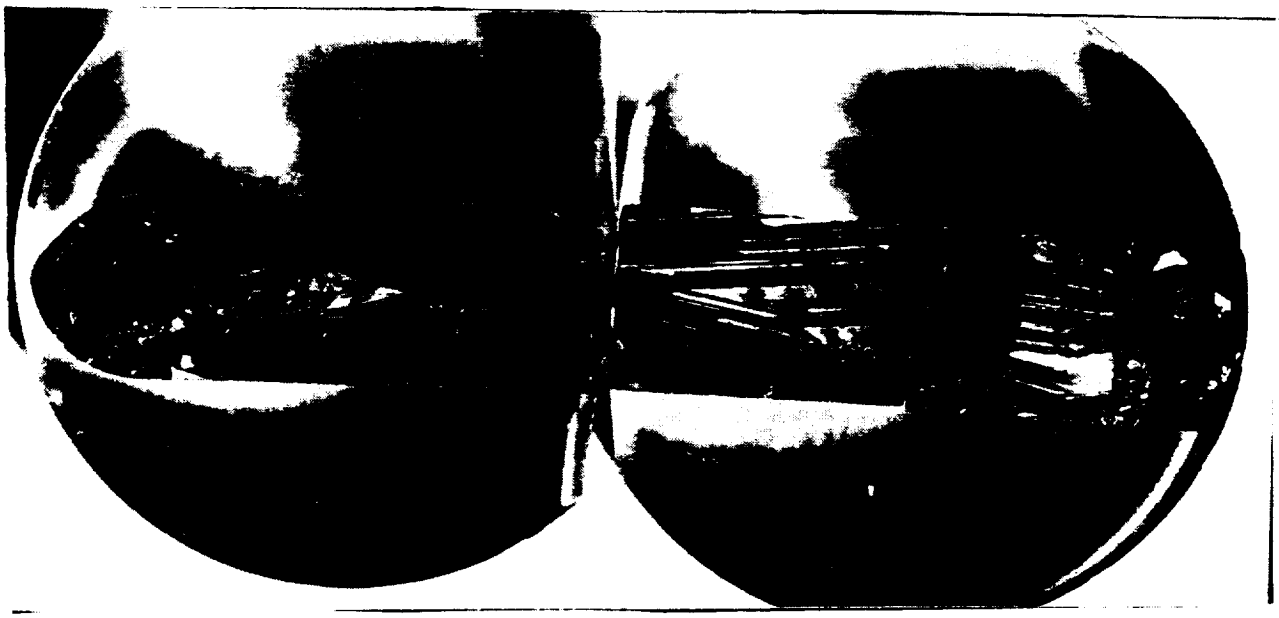

Figure 4.34: Photograph of the microstructure of a longitudinal section of ingot V2, which was solidified with axial vibration of 20 Hz and 0.5 mm amplitude. The structure was revealed by chemically etching the sample in $1HF:1HNO_3:1H_2O$ for 45 sec at room temperature. The samples were cast in a resin mold for polishing. The width of the ingot is 0.9 cm. The growth direction was from left to right.

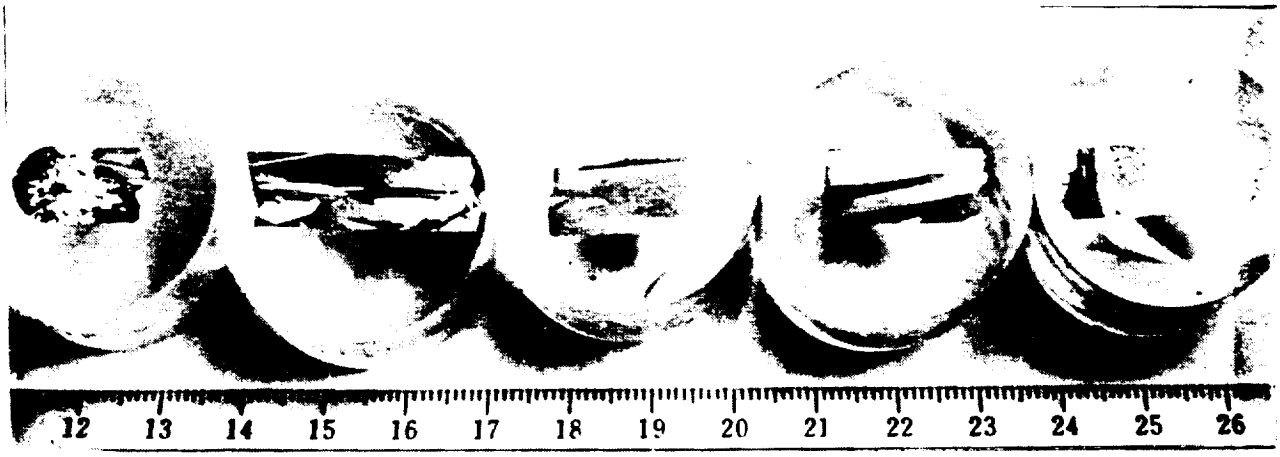

Figure 4.35: Photograph of the microstructure of a longitudinal section of ingot V6, which was solidified with axial vibration of 100 Hz and 0.05 mm amplitude. The structure was revealed by chemically etching in $1HF{:}1HNO_3{:}1H_2O$ for 45 sec at room temperature. The samples were cast in a resin mold for polishing. The last to freeze section shows a quenched liquid-solid interface. The interface was near concave. The width of the ingot is 0.9 cm. The growth direction was from left to right.

4.1.7 Statistical Analysis of Grain and Twin Boundaries

A statistical analysis was performed on the number of curved and straight boundaries in different ingots. The curved and straight boundaries are reported as grain and twin boundaries, respectively, in this work. The number of boundaries per millimeter across an ingot was compared to other ingots. Also the total number of boundaries in each ingot was compared to the other ingots.

The number of grain and twin boundaries was counted across the ingots along the longitudinally sections at 2 mm intervals. Figures 4.36 and 4.37 show the number of grain and twin boundaries per millimeter across the width of the samples for the entire length of the ingots solidified with and without vibration. The number of grain boundaries was significantly lower for the ingots solidified with vibration compared to the one without vibration, especially in the second half of the ingots. The scatter in the data could be due to the presence of small grains along the examined sections. The last half of all ingots showed less scatter in the data as compared to the first half. Figures 4.38 shows the number of grain boundaries for the last half of the ingots.

A one-sided Student's t-test with paired comparisons was used in this analysis. The t-test was performed using a commercially available software package called the Number Cruncher Statistical System (NCSS). A detailed description of the Students's t-test is as follows: Consider two data sets which we desire to compare. Both of these sets are arranged in two columns; the first column lists the length fraction of the ingot solidified and the second column contains the straight boundaries per mm width of ingot. In order to compare them, the two data sets are paired based on equal length fractions of the ingot solidified. These pairs are listed under two columns, C1 and C2 as a separate data set. As described below a the two sided t-test was performed on this data set.

1. Hypothesis proposed: The first step involved the proposal of an hypothesis, which was as follows: To check if the mean of the difference between C1 and C2 is greater than zero.

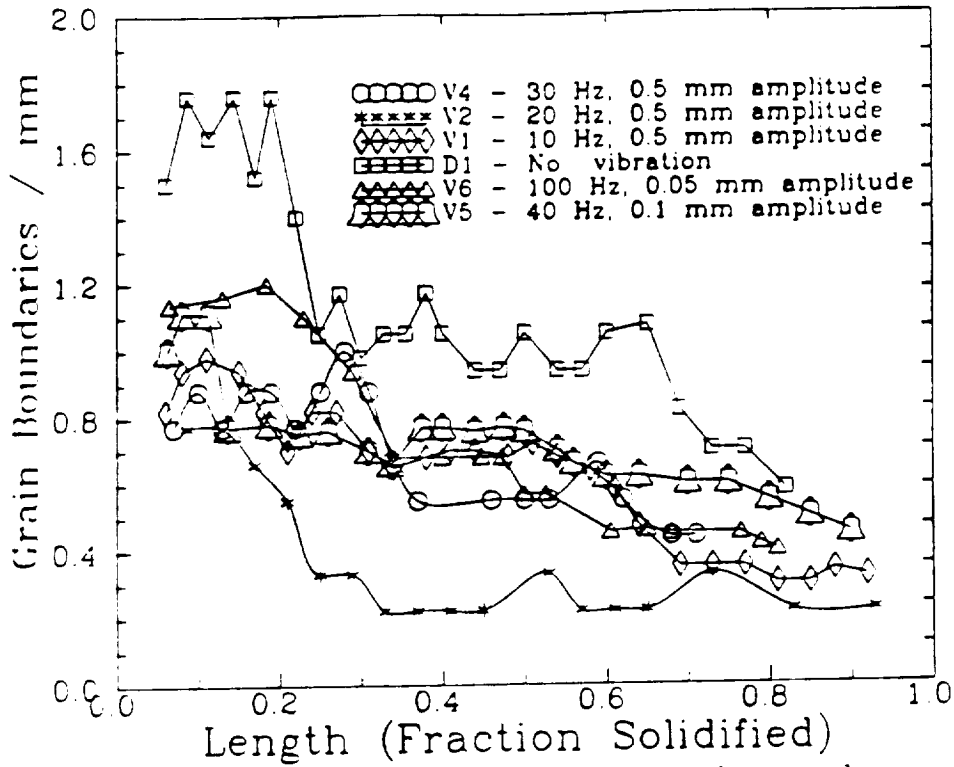

Figure 4.36: Number of grain boundaries per mm counted across the samples at 2 mm intervals along ingots solidified at 8 mm/day translation rate with and without vibration.

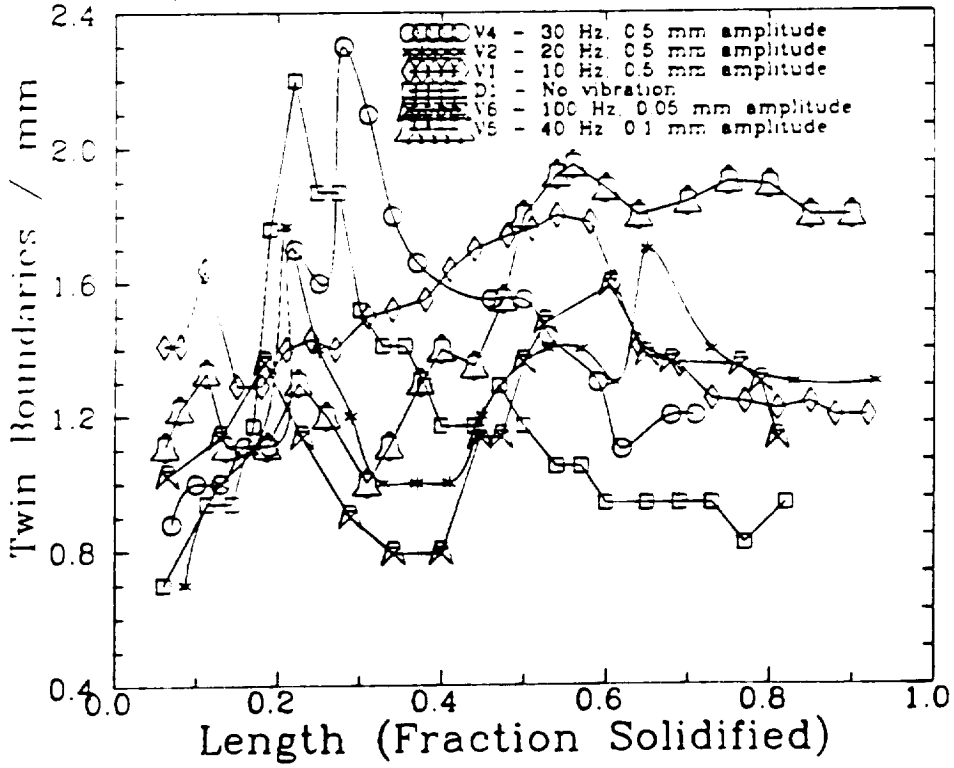

Figure 4.37: Number of twin boundaries per mm counted across the samples at 2 mm intervals along ingots solidified at 8 mm/day translation rate with and without vibration.

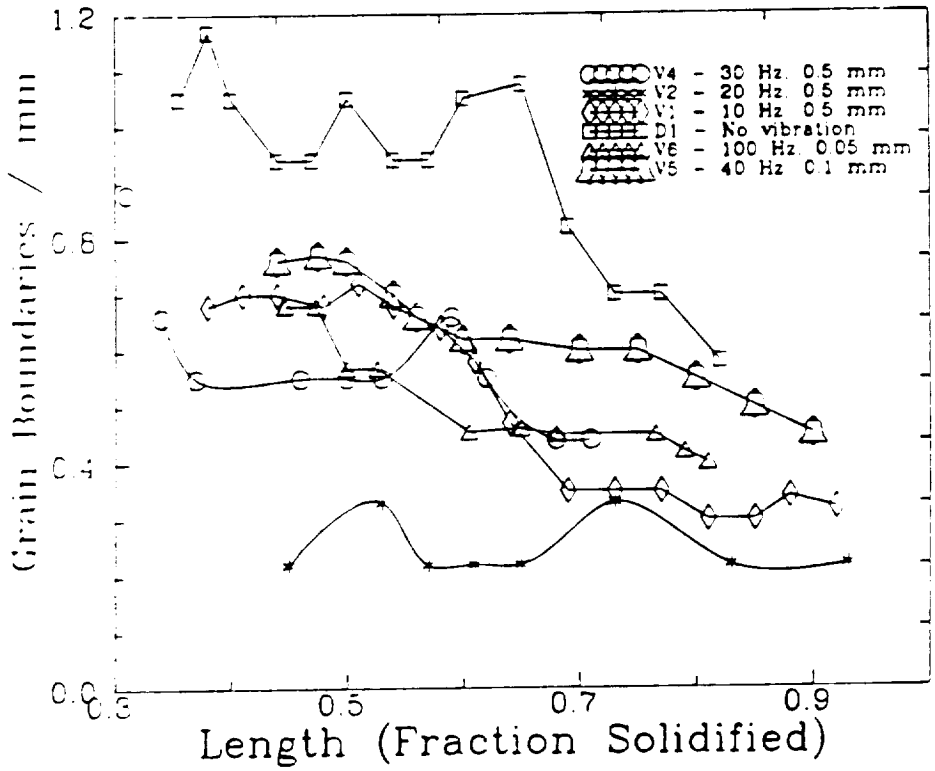

Figure 4.38: Number of grain boundaries per mm counted across the samples at 2 mm intervals along ingots solidified at 8 mm/day translation rate with and without vibration. The boundary counts are for the last half of the ingot.

2. Calculate the differences X_i.

$$X_i = C1_i - C2_i \tag{4.5}$$

3. Calculate the mean difference $\bar{d}$.

$$\bar{d} = \frac{\sum_i^n X_i}{n} \tag{4.6}$$

where n = number of observations.

4. Calculate the variance of the difference s^2.

$$s^2 = \frac{\sum_i^n (X_i - \bar{d})^2}{n-1} \tag{4.7}$$

5. Calculate the standard deviation of the difference s.

$$s = \sqrt{s^2} \tag{4.8}$$

6. Calculate the standard error of the difference $s_{\bar{d}}$.

$$s_{\bar{d}} = \frac{s}{\sqrt{n}} \tag{4.9}$$

7. Calculate the T value t_o.

$$t_o = \frac{\bar{d}}{s_{\bar{d}}} \tag{4.10}$$

8. Calculate the probability level.

$$Probability \quad level = P(|t_o| > 0) \tag{4.11}$$

9. We can say that C1 was greater than C2 at the probability (confidence) level obtained by the previous step.

10. All the above mentioned steps were performed by the NCSS software.

Table 4.2 shows the probability level that the number of grain boundaries (curved) per mm across the ingot, as shown in Figure 4.36, listed in the row was greater than the number of curved boundaries per mm in the ingots listed in the columns of the table. Accordingly, with 99% confidence, ingot D1(no vibration) contained more grain

boundaries per mm than all of the ingots grown with vibration. Ingot V2(20Hz,0.5mm) had the least number of grain boundaries. Ingot V1 (10Hz,0.5mm) and V4 (30Hz,0.5mm) showed similar numbers of grain boundaries, lower than in the ingots V5 and V6.

Table 4.3 shows the probability level that the number of twin boundaries per mm across the ingot, as shown in Figure 4.37, listed in the row was greater than the number of twin boundaries per mm in the ingots listed in the columns. Ingot D1 (no vibration) shows the least number of twin boundaries per mm among all ingots. Ingot V1 (10Hz,0.5mm) and V5 (40Hz,0.1mm) showed the highest number of twin boundaries among all ingots. Ingot V6(100Hz,0.05mm) had the lowest number of twin boundaries among ingots solidified with vibration.

Table 4.4 shows the probability level that the total number of boundaries, i.e. grain and twin boundaries (curved and straight), along the full length, per mm across the ingot listed in the row was greater than the total number of boundaries per mm in the ingots listed in the columns. Ingot D1 (no vibration) showed the highest number of total boundaries per mm among all ingots. Ingot V2(20Hz,0.5mm) solidified with vibration had the lowest number of total boundaries per mm among all ingots. The total number of boundaries per mm in ingot V5(40Hz,0.1mm) was highest among ingots solidified with vibration and comparable with ingot D1 solidified without vibration.

Tables 4.5, 4.6, and 4.7 show the probability level that the number of grain boundaries, twin boundaries, and total number of boundaries along the last half of the ingots listed in the row was greater than the boundaries per mm in the ingots listed in the columns.

The mean of the number of grain and twin boundaries and total boundaries are given in Figures 4.39, 4.40 and 4.41, respectively. The error bars represent the standard error of the means. The standard error of the means is defined as the standard deviation divided by the square root of the total number of observations. The mean of the number of grain boundaries per mm was highest for ingot D1 (no vibration) as compared to all other ingots. Ingot V2 (20Hz,0.5mm) had the lowest mean number of grain boundaries per mm among all ingots. The mean number of twin boundaries per mm was lowest in ingot D1

Table 4.2: Probability level that the number of grain boundaries per mm across the ingot listed in the row was greater than the number of grain boundaries per mm in the ingots listed in the columns. The grain boundaries along the *full length* of the ingots were compared in this table. These ingots were solidified at 8 mm/day translation rate with or without vibration of the ampoule.

Ingot	D1	V1	V2	V4	V5	V6
D1(no vibration)		0.99	0.99	0.99	0.99	0.99
V1(10Hz,0.5mm)			0.99	0.55		
V2(20Hz,0.5mm)						
V4(30Hz,0.5mm)			0.99			
V5(40Hz,0.1mm)		0.99	0.99	0.97		
V6(100Hz,0.05mm)		0.97	0.99	0.97	0.59	

Table 4.3: Probability level that the number of twin boundaries per mm across the ingot listed in the row was greater than the number of twin boundaries per mm in the ingots listed in the columns. The twin boundaries along the *full length* of the ingots were compared in this table. These ingots were solidified at 8 mm/day translation rate with or without vibration of the ampoule.

Ingot	D1	V1	V2	V4	V5	V6
D1(no vibration)						
V1(10Hz,0.5mm)	0.99		0.99	0.72		0.99
V2(20Hz,0.5mm)	0.62				0.75	
V4(30Hz,0.5mm)	0.95		0.95			0.93
V5(40Hz,0.1mm)	0.99	0.62	0.99	0.59		0.99
V6(100Hz,0.05mm)	0.52					

Table 4.4: Probability level that the total number of boundaries per mm across the full length of the ingot listed in the row was greater than the total number of boundaries per mm in the ingots listed in the columns. The total number of boundaries along the *full length* of the ingots were compared in this table. These ingots were solidified at 8 mm/day translation rate with or without vibration of the ampoule.

Ingot	D1	V1	V2	V4	V5	V6
D1(no vibration)		0.93	0.99	0.99	0.68	0.99
V1(10Hz,0.5mm)			0.99	0.71		0.99
V2(20Hz,0.5mm)						
V4(30Hz,0.5mm)			0.99			0.99
V5(40Hz,0.1mm)		0.87	0.99	0.76		0.99
V6(100Hz,0.05mm)			0.99			

Table 4.5: Probability level that the number of grain boundaries per mm across the ingot listed in the row was greater than the number of grain boundaries per mm in the ingots listed in the columns. The grain boundaries along the *last half* of the ingots, as shown in Figure 4.38, were compared in this table. These ingots were solidified at 8 mm/day translation rate with or without vibration of the ampoule.

Ingot	D1	V1	V2	V4	V5	V6
D1(no vibration)		0.99	0.99	0.99	0.99	0.99
V1(10Hz,0.5mm)			0.99	0.55		
V2(20Hz,0.5mm)						
V4(30Hz,0.5mm)			0.99			
V5(40Hz,0.1mm)		0.99	0.99	0.96		0.99
V6(100Hz,0.05mm)		0.68	0.99	0.54		

Table 4.6: Probability level that the number of twin boundaries per mm across the ingot listed in the row was greater than the number of twin boundaries per mm in the ingots listed in the columns. The twin boundaries along the *last half* of the ingots were compared in this table. These ingots were solidified at 8 mm/day translation rate with or without vibration of the ampoule.

Ingot	D1	V1	V2	V4	V5	V6
D1(no vibration)						
V1(10Hz,0.5mm)	0.99		0.96	0.73		0.99
V2(20Hz,0.5mm)	0.92				0.58	0.54
V4(30Hz,0.5mm)	0.99					0.86
V5(40Hz,0.1mm)	0.99	0.98	0.99	0.60		0.99
V6(100Hz,0.05mm)	0.88					

Table 4.7: Probability level that the total number of boundaries per mm across the ingot listed in the row was greater than the total number of boundaries per mm in the ingots listed in the columns. The total number of boundaries along the *last half* of the ingots were compared in this table. These ingots were solidified at 8 mm/day translation rate with or without vibration of the ampoule.

Ingot	D1	V1	V2	V4	V5	V6
D1(no vibration)			0.99	0.98		0.96
V1(10Hz,0.5mm)	0.92		0.99	0.71		0.98
V2(20Hz,0.5mm)						
V4(30Hz,0.5mm)			0.95			0.89
V5(40Hz,0.1mm)		0.99	0.99	0.72		0.99
V6(100Hz,0.05mm)			0.99			

(no vibration) among all ingots, especially in the last half of the ingots, as shown in Figure 4.43. The total number of boundaries was lowest in ingot V2(20Hz,0.5mm) and highest in ingot V5(40Hz,0.1mm). The high number of total boundaries in ingot V5 was due to large number of twin boundaries.

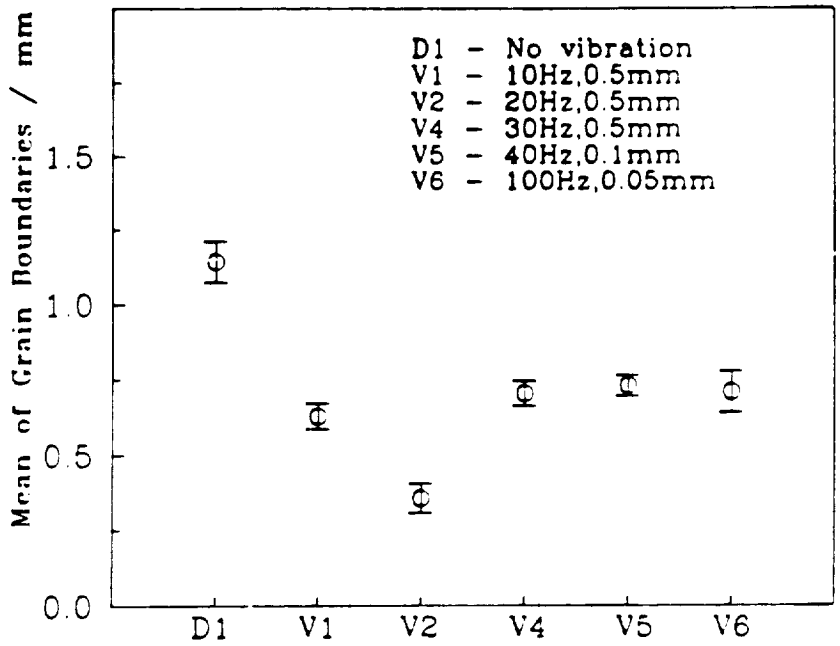

Figure 4.39: Mean number of grain boundaries per mm width counted across the samples at 2 mm intervals along full length of the ingots solidified with and without vibration at 8 mm/day translation rate. The error bars represent the standard error of the mean.

Figures 4.44 and 4.45 show the mean number of grain and twin boundaries per mm of the ingots solidified with and without vibration versus the vibration-induced dynamic acceleration. The acceleration was measured using an accelerometer during application of vibration. The ± accelerations represent the maximum and minimum acceleration values measured at specific vibration conditions. The dynamic acceleration variations followed a sinusoidal harmonic pattern (refer to Acceleration Measurement section in the Results chapter for more detail). The mean number of grain boundaries was highest for 1g(gravitational acceleration without vibration). The mean number of grain boundaries decreased as the dynamic acceleration increased up to ±0.18, for ingot V2(20Hz,0.5mm). A higher dynamic acceleration of ±0.25 (ingot V4 - 30 Hz,0.5mm) showed an increase in the number of grains compared to the other ingots grown with vibration; still the number of grain boundaries

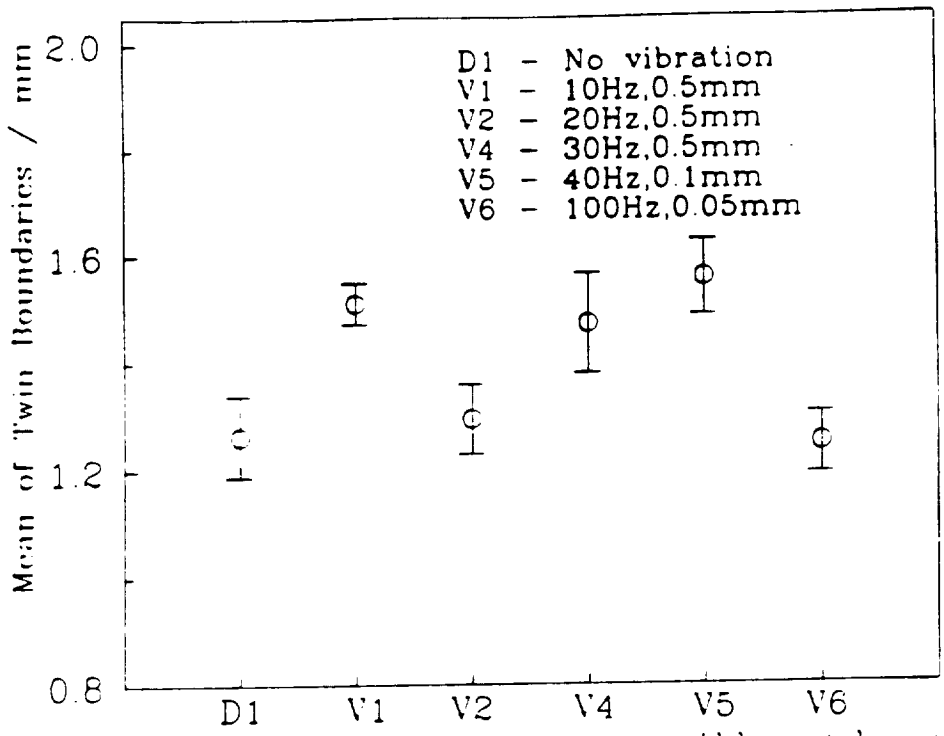

Figure 4.40: Mean number of twin boundaries per mm width counted across the samples at 2 mm intervals along full length of the ingots solidified with and without vibration at 8 mm/day translation rate. The error bars represent the standard error of the mean.

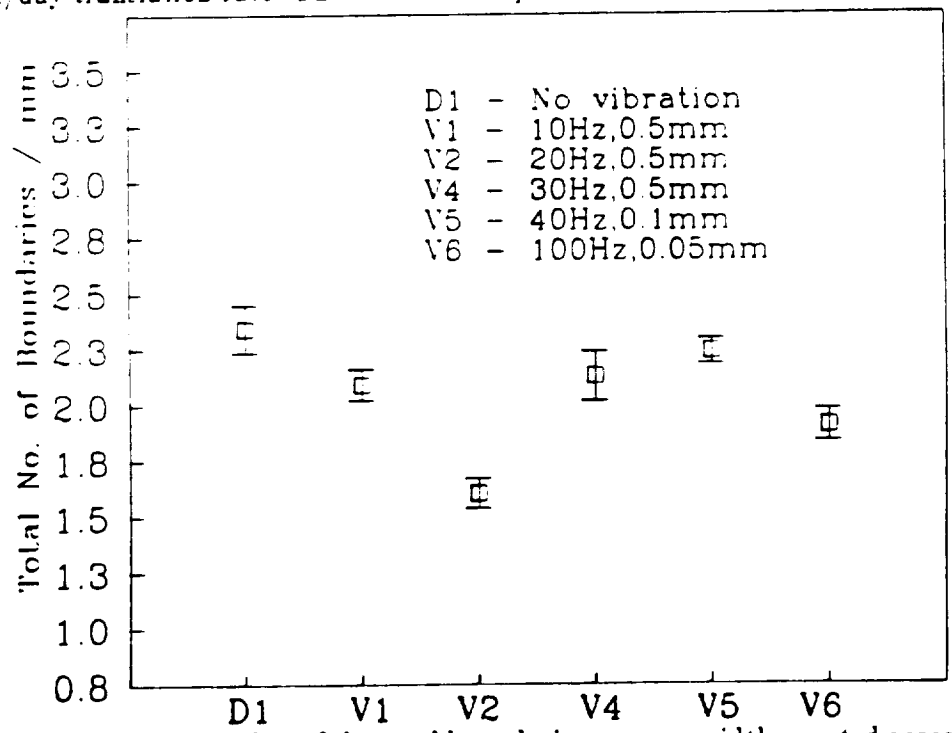

Figure 4.41: Mean number of the total boundaries per mm width counted across the samples at 2 mm intervals along the full length of the ingots solidified with and without vibration at 8 mm/day translation rate. The error bars represent the standard error of the mean.

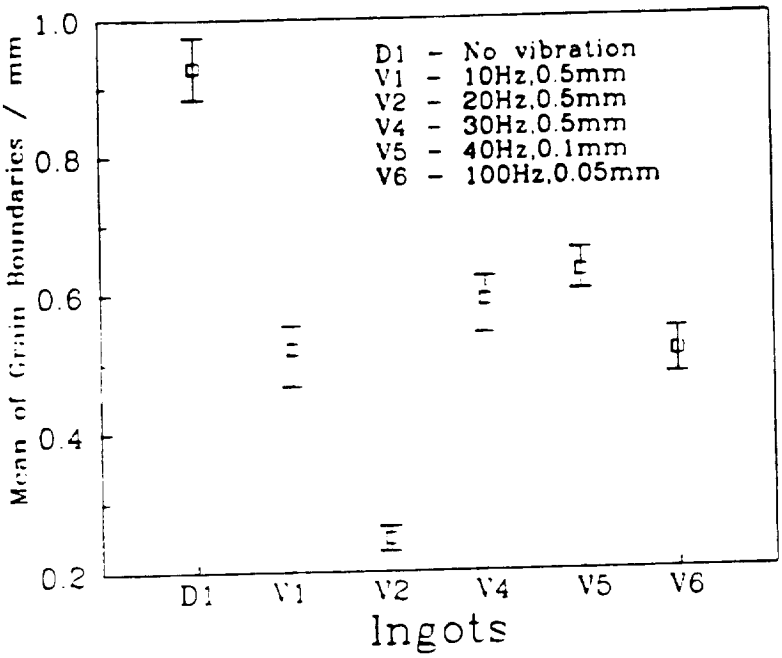

Figure 4.42: Mean number of grain boundaries per mm width counted across the samples at 2 mm intervals along last half of the ingots solidified with and without vibration at 8 mm/day translation rate. The error bars represent the standard error of the mean.

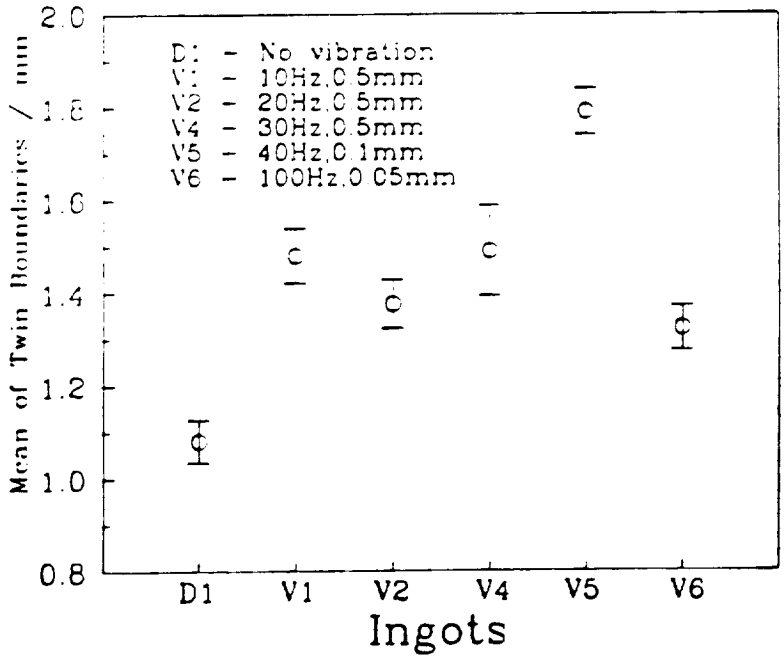

Figure 4.43: Mean number of twin boundaries per mm width counted across the samples at 2 mm intervals along last half of the ingots solidified with and without vibration at 8 mm/day translation rate. The error bars represent the standard error of the mean.

was lower than in the ingot grown without vibration.

The mean number of twin boundaries in the ingots did not follow a well-defined pattern with respect to the dynamic acceleration. However, the mean number of twin boundaries was lowest for ingot D1(no vibration) as compared to ingots grown with vibration.

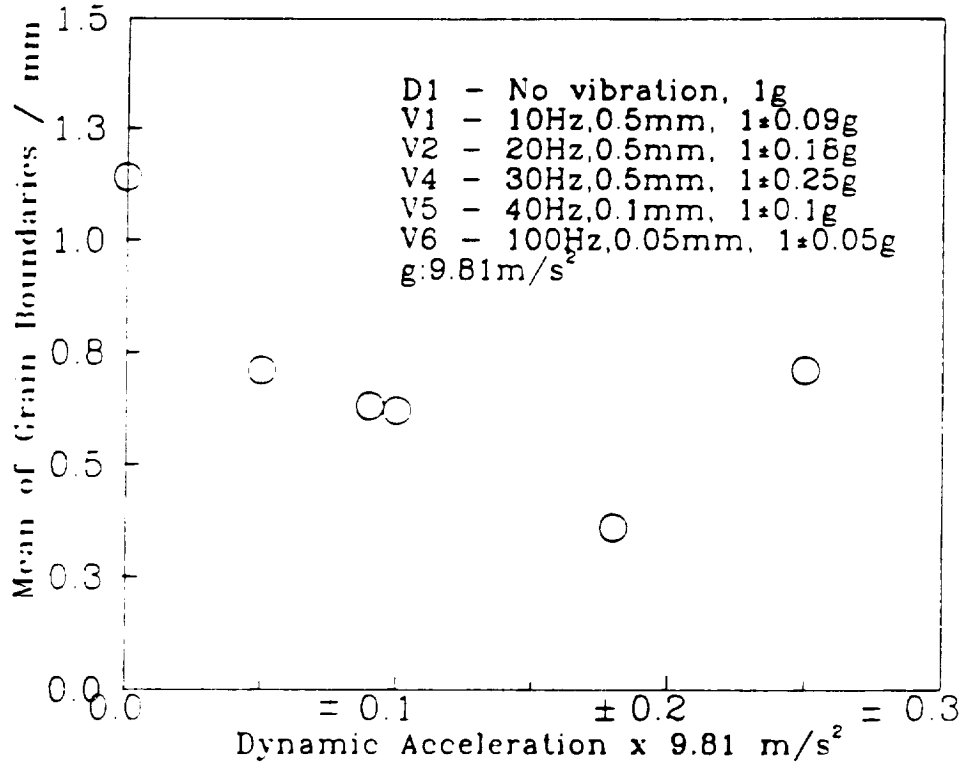

Figure 4.44: Mean number of grain boundaries per mm of the ingots solidified with and without vibration at 8 mm/day translation rate. The grain boundary counts are plotted versus the dynamic acceleration induced by vibration during growth. For example, the zero acceleration is for run D1 without vibration and ±0.05g represents the minimum and maximum dynamic accelerations during growth of ingot V6.

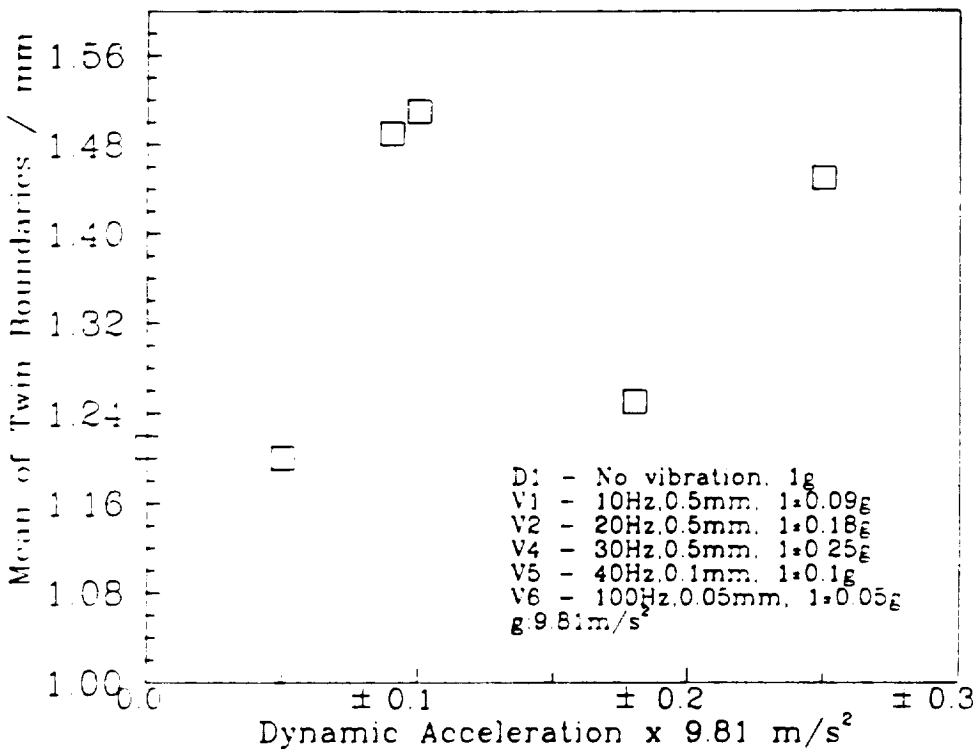

Figure 4.45: Mean number of twin boundaries per mm of the ingots solidified with and without vibration at 8 mm/day translation rate. The twin boundary counts are plotted versus the dynamic acceleration induced by vibration during different growth runs. For example, the zero acceleration is for run D1 without vibration and the ±0.05g represents the minimum and maximum dynamic acceleration during growth of ingot V6.

4.2 Current-induced Perturbations Studies

In this section the results of a solidification run with passage of alternating current through the ampoule, current interface demarcation of Te-doped $In_{0.2}Ga_{0.8}Sb$ ingot, and *in-situ* temperature measurements in the melt and in the vicinity of liquid-solid interface of GaSb and InGaSb charge are presented and discussed.

4.2.1 Solidification with Alternating Current

An ingot with $In_{0.2}Ga_{0.8}Sb$ initial feed composition was directionally solidified at 8 mm/day ampoule translation rate and 25-30°C/cm axial temperature gradient (measured in an empty ampoule) with application of alternating 15 amp/cm^2 current pulses. The passage of current through the growth system was started after 72 hours of ampoule lowering. The current was applied alternatively with 25 sec (+) and 25 sec (-) polarities during growth. The 25 sec puse duration was similar to one of the ACRT experiments performed by Gray [20] at Clarkson. The original objective of this experiment was to compare an ingot solidified with ACRT at 25 sec cycle time to an ingot grown with current pulses of 25 sec duration. The common point between the ACRT and current-induced growth was the possibility of backmelting and regrowth behavior. The magnitude of periodic growth for InSb-GaSb under application of ACRT or electric current is not available.

Figure 4.46 shows a photograph of the longitudinal section of this ingot. The sample was sandblasted to reveal the microstructure. This ingot had a much finer grain structure with microcracks than the ingot shown in Figure 4.47, solidified without current pulses under otherwise identical growth conditions.

The axial and radial compositional profiles of ingots were measured using EDS (details described in Experimental section). Axial composition profiles of the above two ingots are shown in Figure 4.48 and 4.49. The cross-sectional composition profiles of these ingots are shown in Figures 4.50 and 4.51. The ingot solidified without current shows an axial composition profile corresponding to good mixing in the melt and uniform radial composition at different positions in the ingot. On the other hand, the ingot C1 solidified with current shows significant axial and radial compositional variations. The radial composition

in the initial section, up to about g=0.12, of ingot C1 is fairly uniform. This section of the ingot was directionally solidified without current.

The microcracks in ingot C1 were possibly due to stress induced by compositional variations. The fine grain structure, microcracks, and compositional fluctuations in ingot C1, which was solidified with current pulses, are indicative of morphological breakdown caused by passage of current. The criterion for occurrence of constitutional supercooling in a binary alloy with and without application of electric current is formulated and given in Appendix A.

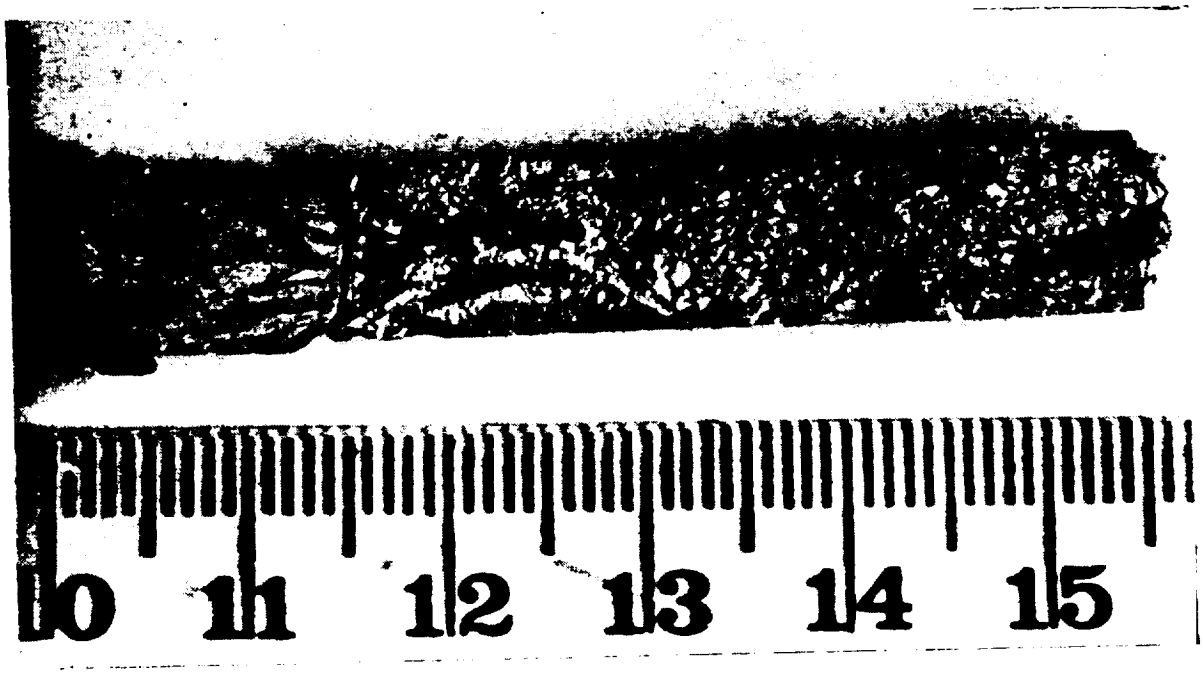

Figure 4.46: Longitudinal section of an ingot with feed composition $In_{0.2}Ga_{0.8}Sb$ frozen at a translation rate of 8 mm/day with application of alternating 15 amp/cm^2 current. The ingot was sandblasted to reveal the microstructure. The microstructure exhibits a fine grain structure with microcracks. The growth direction was from left to right.

From Appendix A, a heat balance at the interface can be written with and without current applied:

$$k_s G_s - k_l G_l = V_{nc} H \quad (No\ Current) \tag{4.12}$$

$$k_s G_s - k_l G_l = (V_{nc} + V_c) H + \pi I \quad (With\ Current) \tag{4.13}$$

Figure 4.47: Longitudinal section of an ingot with feed composition $In_{0.2}Ga_{0.8}Sb$ directionally frozen at an ampoule translation rate of 8 mm/day without application of current. The ingot was chemically etched in $1HF:1HNO_3:1H_2O$ solution for 20 sec at room temperature to reveal the microstructure. This ingot consists of several twinned grains. The growth direction was from left to right.

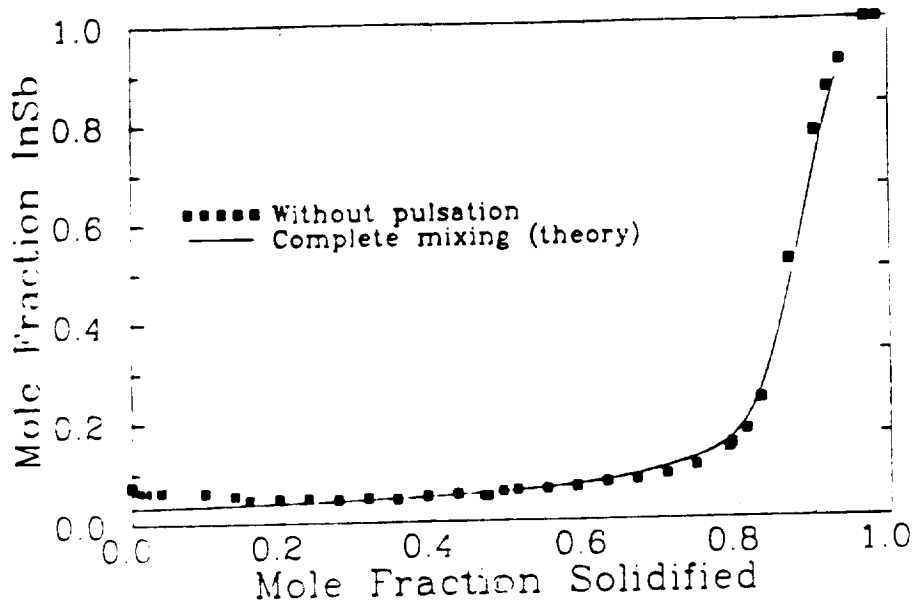

Figure 4.48: Axial compositional profiles of an ingot directionally solidified without application of current. The profile corresponds to good mixing in the melt.

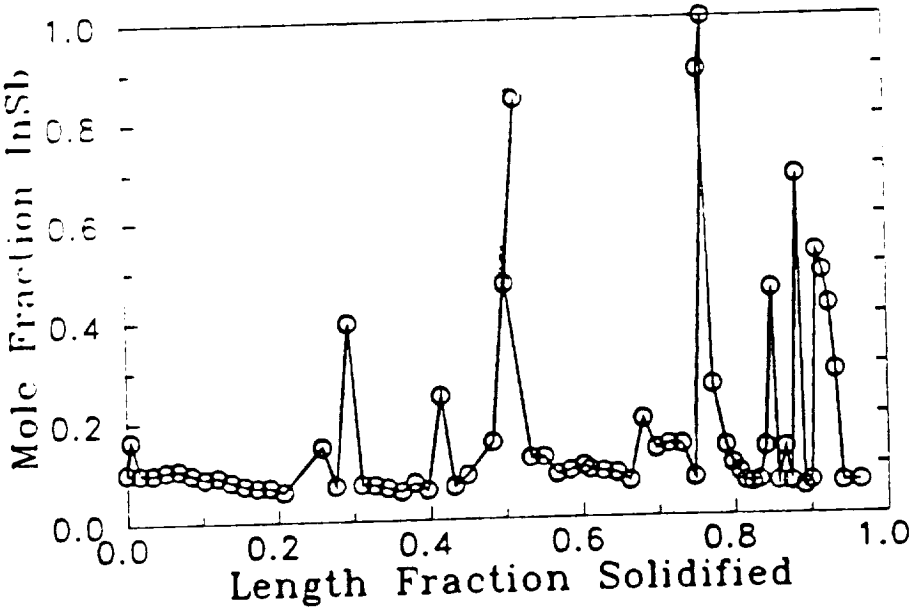

Figure 4.49: Axial compositional profile of an ingot solidified with alternating 15 amp/cm^2 current pulses. Current was applied after initial 4 days of ampoule lowering corresponding.

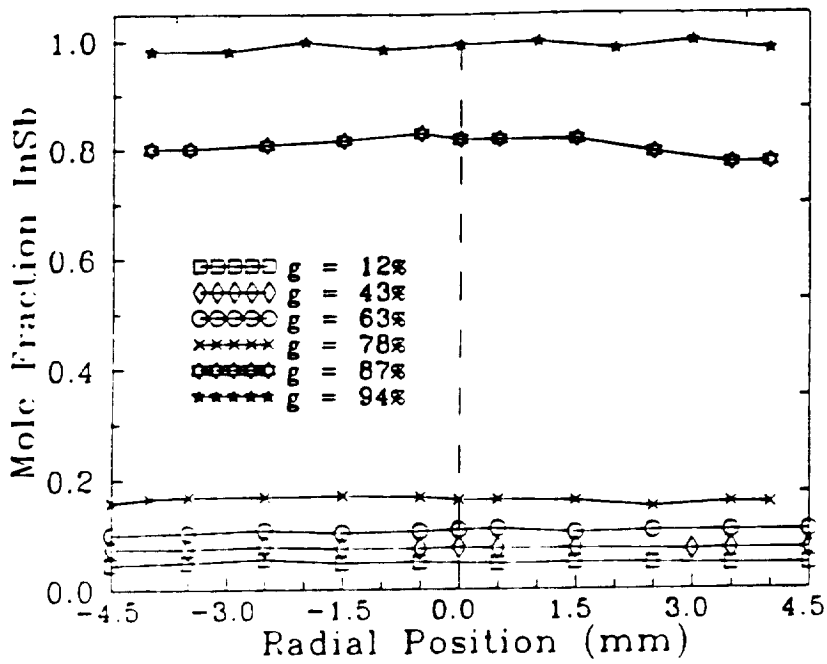

Figure 4.50: Radial compositional profiles of the ingot directionally solidified without application of current. Here g is the longitudinal mole fraction down the ingot.

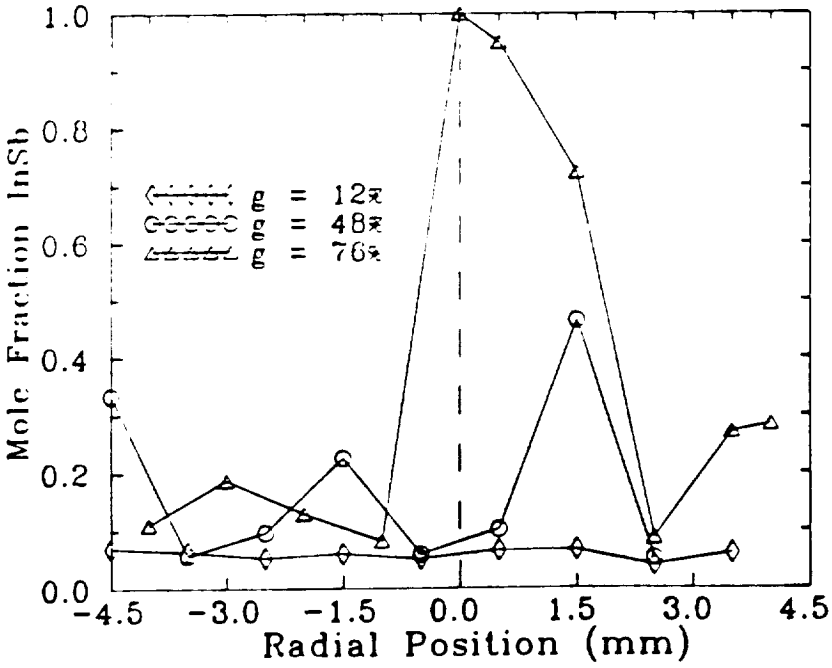

Figure 4.51: Radial compositional profiles of the ingot C1 solidified with application of current. Here g is the axial position expressed as mole fraction of the ingot solidified.

where V_c is the interface velocity without current applied, G_s and G_l are the axial temperature gradients in the solid and liquid at the interface, respectively, π is the Peltier coefficient, H is the heat of fusion per unit volume, and J is the current density. The net velocity during passage of current is $(V_{nc} + V_c)$. The perturbation in temperature gradients is negligible at the instant of application of current. At that instant the current-induced change in growth rate is, from the above equations:

$$V_c = \frac{-\pi J}{H} \tag{4.14}$$

Equations describing the conditions for avoidance of constitutional supercooling are given as (see Appendix A for more details):

$$(No\ Current)\ \ G_{lcritical} \geq \frac{X_l m}{D}\frac{C_c}{C_f}[V_{nc}(k_t - 1)] \tag{4.15}$$

At the first instant when current is turned on:

$$G_{lcritical} \geq \frac{X_l m}{D}\frac{C_c}{C_f}[(V_{nc} - \frac{\pi J}{H})(k_t - 1) - U(\rho J)] \tag{4.16}$$

where m is the slope of liquidus curve, k_t is the interfacial distribution coefficient determined from phase diagram, C_c and C_f are the total molar concentration of solute in the solid and in the liquid at the interface, respectively, U is the electromobility, ρ is the electrical resistivity, and J is the current density.

The above equations were used to estimate the critical temperature gradient $G_{lcritical}$ as a function of composition for $In_xGa_{1-x}Sb$.

In this work $In_{0.2}Ga_{0.8}Sb$ feed composition was used for all directional solidification experiments both with and without current pulsations. Fitting the liquidus curve for the phase diagram of InSb-GaSb, shown in Figure 4.52, we obtain:

$$T = 709.5 - 93.1X_l - 96.1X_l^2 \tag{4.17}$$

where X_l is the mole fraction of InSb. The slope of the liquidus is determined by differentiation of the above equation as:

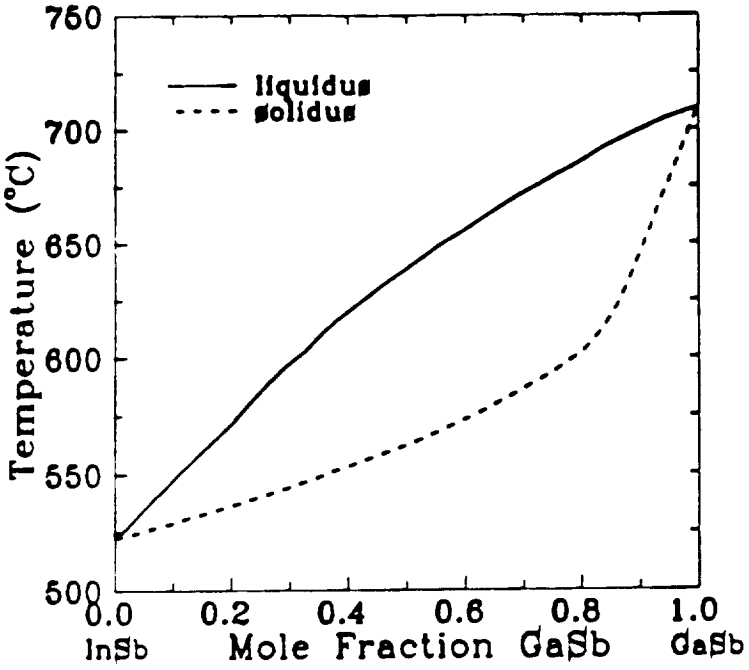

Figure 4.52: Equilibrium phase diagram of InSb-GaSb system [50].

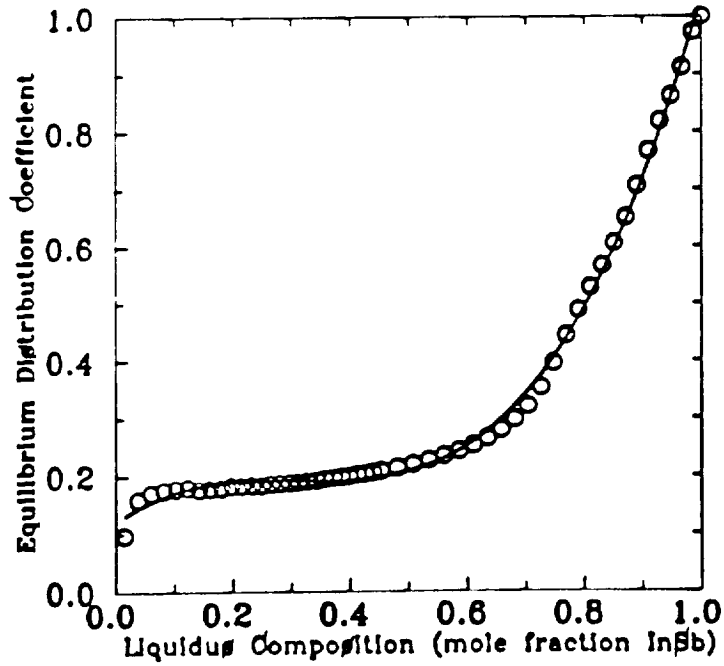

Figure 4.53: Equilibrium distribution coefficient k_o versus mole fraction X_l liquidus concentration of InSb for InSb-GaSb system. The circles are the data taken from the phase diagram. The line is a polynomial fit given as $k_o = \frac{X_s}{X_l} = 0.12 + 0.721X_l - 2.37X_l^2 + 2.57X_l^3$.

$$m = \frac{dT}{dX_l} = -93.1 - 192.2X_l \tag{4.18}$$

From the phase diagram, the equilibrium distribution coefficient k_o is determined as a function of the liquidus composition of InSb, as shown in Figure 4.52:

$$k_o = \frac{X_s}{X_l} = 0.12 + 0.721X_l - 2.37X_l^2 + 2.57X_l^3 \tag{4.19}$$

where X_s is the mole fraction of solute in the solid at the interface. Assuming that equilibrium prevails at the interface, the interfacial distribution coefficient is the same as the equilibrium distribution coefficient, i.e., $k_i = k_o$.

The thermophysical properties of $In_xGa_{1-x}Sb$ are not known versus composition. The properties of InSb and GaSb are fairly well determined and are given in Appendix C. Here in our calculations we used properties for GaSb, such as Peltier coefficient (π_{GaSb}=0.06 volt), latent heat of fusion (H_{GaSb}=1300 J/cm^3), and resistivity (ρ=0.001 Ω.cm). For estimation of the critical G_l the growth rate without application of current was set to the ampoule lowering rate of 8 mm/day, which is 9.25 $\times 10^{-6}$ cm/s.

In principle, electromigration in a ternary system, such as molten In-Ga-Sb, cannot be described correctly using a formulation for a binary system. In molten In-Ga-Sb, the stochiometric $(In + Ga)/Sb$ will not be maintained in the presence of diffusion and electromigration. However, there is no information available on electromigration or diffusion in molten In-Ga-Sb in the literature. In the absence of data on ternary transport properties, we assumed that the stoichiometry is maintained as a pseudo-binary mixture of InSb and GaSb, recognizing that the results are only approximate. InSb is considered to be the solute. The electromobility coefficient U is assumed to be the relative migration between InSb and GaSb in the presence of an applied electric field. Values of D=2x10^{-5} cm^2/s and U=1x10^{-4} cm^2/s.volt were used. These are within the range of the values for metallic melts [80].

In Figure 4.54 the critical temperature gradient G_l is plotted versus the mole fraction of InSb for the InSb-GaSb system. As noted above, this plot is not valid to quantify the effect of electromigration in the InSb-GaSb system. It is used only to qualitatively

demonstrate the effect of electromigration in a pseudo-binary system. Note that the electromigration induced by a current density of 15 amp/cm^2 is not predicted to show a significant effect on the critical temperature gradient, especially at lower values of mole fraction.

Figure 4.55 shows a plot of critical temperature gradient including the Peltier effect, induced by application of -15 amp/cm^2 current density. The electromigration term was neglected. The negative polarity current results in Peltier cooling at the interface, therefore momentarily increasing the rate of growth. Due to application of -15 amp/cm^2 current, the instantaneous current-induced growth increase is estimated to be:

$$V_c = \frac{-\pi I}{H} = 0.0007 \ \ cm/s \qquad (4.20$$

Comparing the growth rates with and without current-induced Peltier cooling we find:

$$\frac{V_c + V_{ns}}{V_{ns}} = \frac{0.0007}{0.000009} = 70 \qquad (4.21$$

Thus at the initial instant of Peltier cooling, the interfacial velocity is estimated to be about 70 times higher than before the current was applied. During application of current the thermal field in the melt and solid changes. Consequently the interfacial velocity should decrease from its initial sudden rise and approach the rate before application of current.

Brush et al. [91] calculated the interfacial velocity for solidification of InSb during application of electric current (discussed in detail in the section on Current-induced Perturbations). For repeated current pulses of 9.5 amp/cm^2 on for 20 sec and off for 40 sec, as shown in Figure 4.56, the interfacial velocity was predicted to suddenly increase from 10 micron/sec ampoule lowering rate to 18.5 micron/sec. Due to thermal relaxation, the interface velocity was predicted gradually to decrease and then suddenly to fall to below the ampoule translation rate when the current is turned off.

The estimated 70 fold increase in freezing rate caused by application of current during solidification of InSb-GaSb alloy system would require a very high temperature gradient to avoid constitutional supercooling. In our work an imposed temperature gradient of less than 25-30 °C/cm was used in the directional solidification of InSb-GaSb ingots (discussed in detail in the Experimental section). Although this is below the gradient

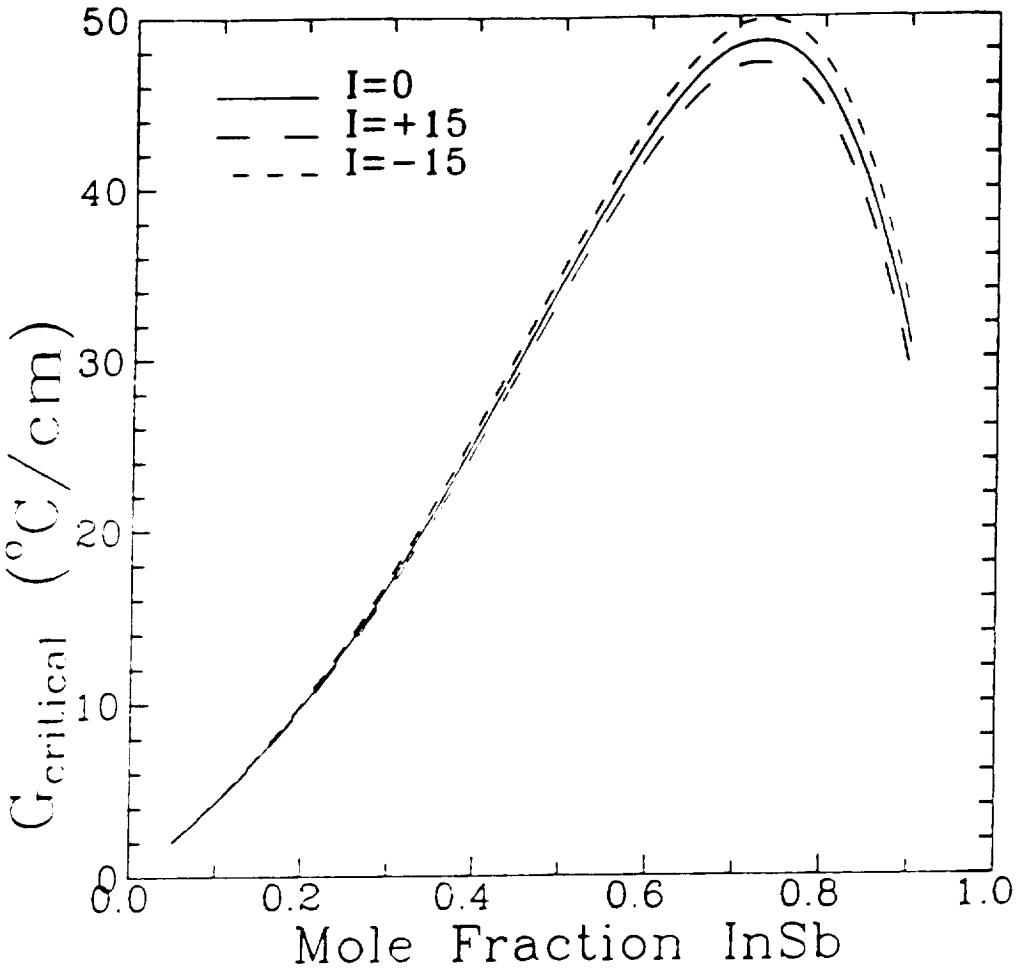

Figure 4.54: Plot of critical temperature gradient versus liquid composition for InSb-GaSb system with current-induced electromigration. These parameters were used; $D=2\times10^{-5}$ cm^2/s, $H_{GaSb}=1300$ J/cm^3, $\rho=0.001$ Ω.cm, $U=1\times10^{-4}$ $cm^2/s.volt$ and $V_{nc}=9.25\times10^{-6}$ cm/s (8 mm/day). Only the electromigartion term was considered. The Peltier term was neglected. The curves represent the cases for 1) I=0 no current-induced effect, 2) I=+15 amp/cm^2 current density, and 3) I=-15 amp/cm^2 current density. Above the curves it is stable condition and below the curves, it is unstable.

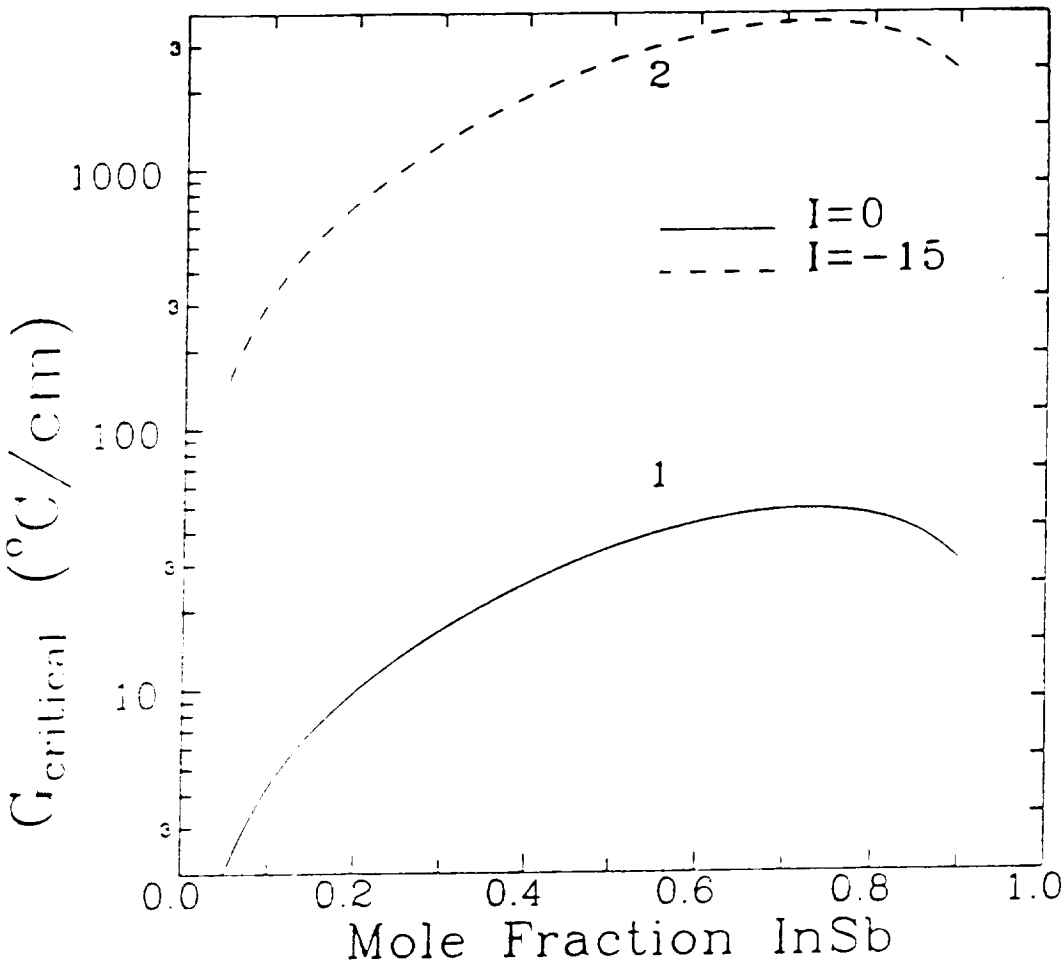

Figure 4.55: A semi-log plot of critical temperature gradient versus liquid composition for InSb-GaSb system with current-induced Peltier cooling. These parameters were used $D=2\times10^{-5}$ cm^2/s, $H_{GaSb}=1300$ J/cm^3, $\rho=0.001$ Ω.cm, $V_{nc}=9.25\times10^{-6}$ cm/s (8 mm/day), and $\pi_{GaSb}=0.06$ volt. Only the Peltier term was considered. The electromigration term was neglected. The curves represent the cases for; 1) I=0 no current-induced effect, 2) I=-15 amp/cm^2 current density (Peltier cooling effect). Above the curves, interface is stable and below the curve, it is unstable.

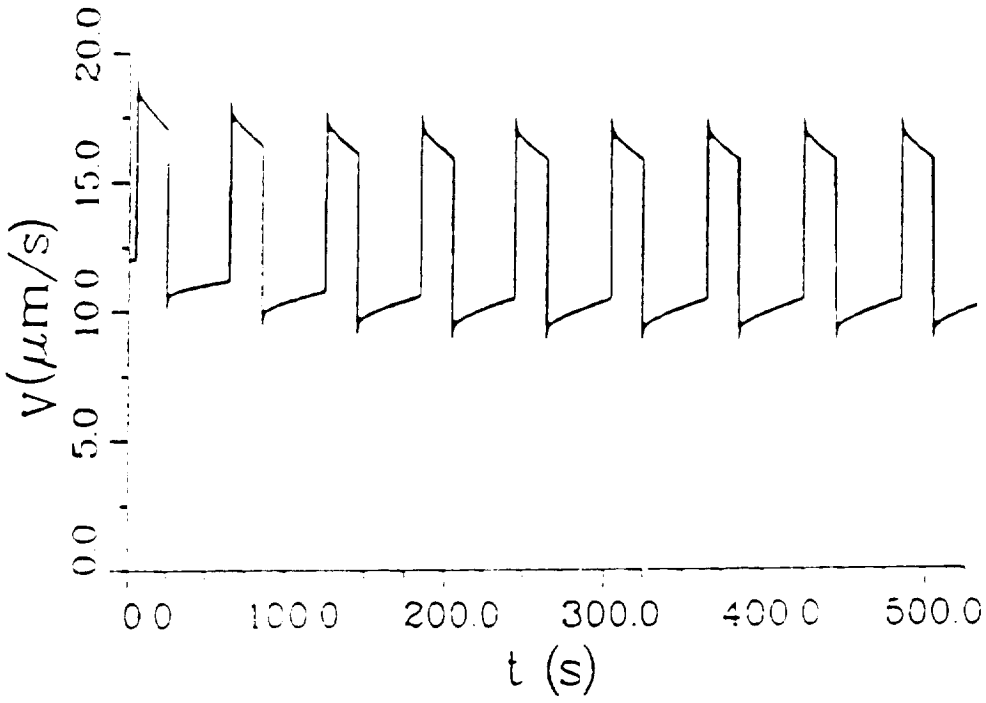

Figure 4.56: Plot of calculated interfacial velocity as a function of time for InSb during periodic application of 9.5 amp/cm^2 current for 20 sec on and 40 sec off [91].

required to avoid constitutional supercooling, the interface may not break down during a pulse. Instead new grains and twins may nucleate in the momentarily supercooled melt, before the interface can change shape. This may result in formation of fine grain structure and cellular growth. In our growth experiment with applied current the microstructure of the ingot consisted of fine grains with significant compositional fluctuations.

4.2.2 Current Interface Demarcation of Te-doped $In_{0.2}Ga_{0.8}Sb$

A current interface demarcation experiment was performed with $In_xGa_{1-x}Sb$ doped with tellurium. A 7 cm long by 9 mm diameter charge of $In_{0.2}Ga_{0.8}Sb$ was alloyed in the rocking furnace for 9 hours at 820°C. The charge was placed in an electroded ampoule and 1000 ppm by weight of six-nines purity tellurium was added to the charge. The ampoule was purged with argon and sealed under a vacuum of 10^{-6} torr. The ampoule was placed in the Bridgman-Stockbarger furnace with settings of 800°C and 475°C for heater and cooler, respectively, and a 5 cm long adiabatic zone. The charge was allowed to melt down aand left over night. The ampoule was occasionally shaken manually for homogenization of Te dopant in the melt. The ampoule was lowered at 8 mm/day.

After solidification, the resulting ingot was sectioned longitudinally, cast in a resin mold, and mechanically polished. These samples were chemically etched in 1HF : $1HNO_3$: $1KMnO_4$ solution for 60-80 sec at room temperature, and rinsed in de-ionized water and methanol. The samples were examined using darkfield and Nomarski optical microscopy and scanning electron microscopy. Current-induced growth rate variations manifested themselves in the ingot as Te concentration bands known as pulse striations [25]. The Te-rich regions were preferentially etched, resulting in bands with different topography compared to the regions solidified without current.

A series of 10 amp current pulses with 10 sec on-time and 300 sec off-time duration were tried. The current was passed from solid (+) to melt (-). The current pulses were passed during the last 5 days of growth. The ingot had a poor microstructure with microcracks and many small grains. Striations were oberved in some grains and not in others. Consequently, it was difficult to trace these striations to determine the overall shape of the liquid-solid interface at the time of a pulsation.

Figure 4.57 shows a scanning electron micrograph of pulsed striations in $In_{0.2}Ga_{0.8}Sb$ feed composition ingot doped with tellurium. These striations were generated by passage of 10 amp current (15.7 amp/cm^2) for 10 sec followed by no current for 300 sec. The current was passed from solid (+) to melt (-). The groved boundary is a grain boundary with the interface demarcations crossing the boundary. Interestingly, the demarcations were ir-

regular in the vicinity of some boundaries. Figures 4.58 and 4.59 show photomicrographs of striations across straight and curved boundaries. These photomicrographs were taken using Nomarski optical microscopy with polarized light. A closer examination of the curved boundary in Figure 4.58 shows that the boundary was wiggly. The frequency of striations corresponded to the frequency of the wiggle. Some irregularities in demarcated regions were observed in the vicinity of the wiggled, curved boundary.

Figure 4.60 shows a photomicrograph of striations crossing a twin boundary in Te-doped $In_{0.2}Ga_{0.8}Sb$ generated by passage of 10 amp current from solid (+) to melt (-) for 10 sec followed by no current for 300 sec. The striations were revealed by etching of the sample in $1HF:1HNO_3.1KMnO_3$ solution for 1 min at room temperature. The photomicrograph was taken using Nomarski optical microscopy with polarized light. The demarcations were regular across the twin boundaries. No sign of instability or irregularity was observed in the demarcation across the twin boundaries. A slightly shift of demarcation position was observed with twinned regions, as seen in Figure 4.60.

Figure 4.57: Scanning electron micrograph of striations in a Te-doped $In_{0.2}Ga_{0.8}Sb$ ingot. A 10 amp current was passed from solid (+) to melt (-) for 10 sec followed by 300 sec without current. The sample was etched in $1HF:1HNO_3:1KMnO_3$ solution for 1 min at the room temperature. The magnification is 500X. The long scale bar, pointed at with a small arrow, is 10 micron. Direction of growth was as shown by the long arrow in the right upper right-hand corner of the picture.

Figure 4.58: Photomicrograph of striations in a Te-doped $In_{0.2}Ga_{0.8}Sb$ ingot generated by passage of 10 amp current from solid (+) to melt (-) for 10 sec followed by no current for 300 sec. The striations were revealed by etching the sample in $1HF:1HNO_3.1KMnO_3$ solution for 1 min at room temperature. This photomicrograph was taken using Nomarski optical microscopy with polarized light. Note that the striations cross one curved and one straight boundary. The magnification was 100X. The direction of growth was from bottom to top of the picture.

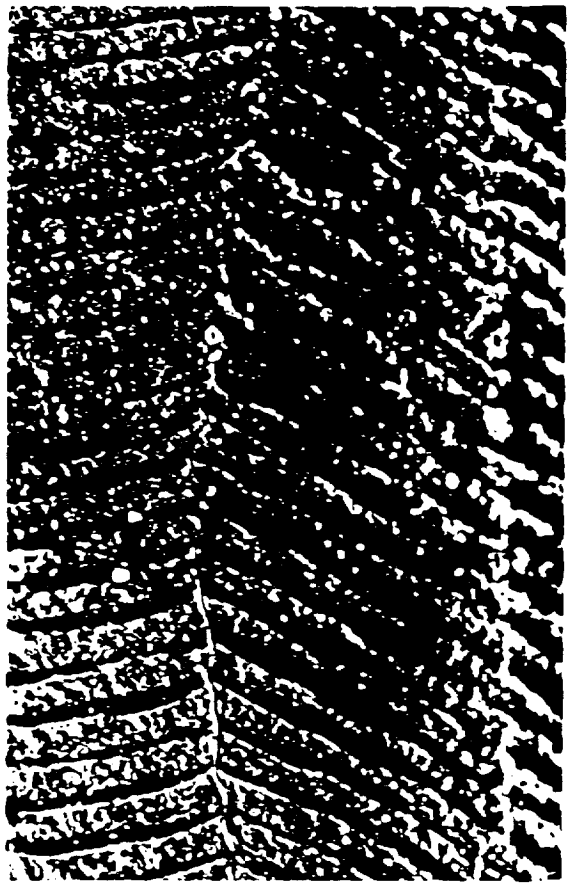

Figure 4.59: Photomicrogrpah of irregular striations in a Te-doped $In_{0.2}Ga_{0.8}Sb$ ingot generated by passage of 10 amp current from solid (+) to melt (-) for 10 sec followed by no current for 300 sec. The striations were revealed by etching the sample in $1HF:1HNO_3.1KMnO_3$ solution for 1 min at room temperature. This photomicrograph was taken using Nomarski optical microscopy with polarized light. Note the irregularity in the striations near the boundary. The magnification is 200X. The direction of growth was bottom to top of the picture.

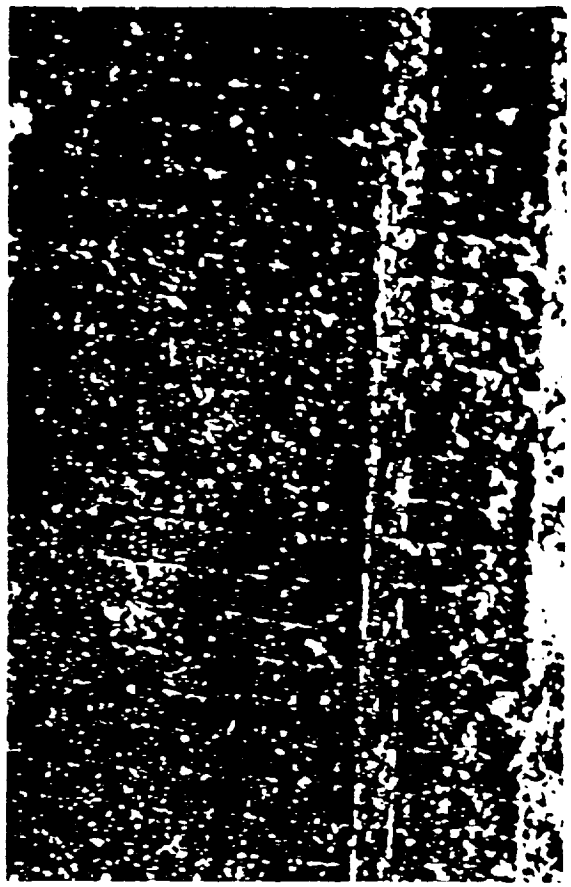

Figure 4.60: Photomicrograph of striations crossing a twin boundary in Te-doped $In_{0.2}Ga_{0.8}Sb$ generated by passage of 10 amp current from solid (+) to melt (-) for 10 sec followed by no current for 300 sec. The striations were revealed by etching of the sample in $1HF:1HNO_3.1KMnO_3$ solution for 1 min at room temperature. The Photomicrograph was taken using Nomarski optical microscopy with polarized light. The direction of growth was from bottom to top of the picture. magnification was 225X.

4.2.3 *In-situ* Temperature Measurements with Current

Passage of current through a melt-solid system results in Peltier heating or cooling at the interface, Joule heating, and Thomson heating or cooling in the solid and melt. These thermoelectric effects cause transient thermal perturbations in the melt and solid. The magnitude of the thermal perturbations depends on the magnitude and direction of the current(for reversible Peltier and Thomson heating or cooling). In semiconductor materials, the Peltier effect depends on the electronic behavior of materials. For example, in n-type materials such as InSb (intrinsicly n-type), passage of current from melt(+) to solid(-) results in Peltier heating. By changing the direction of current, Peltier cooling results. Whereas in p-type materials such as GaSb, the effect of application of current at the melt - solid interface is opposite to n-type materials.

An alloy of InSb-GaSb changes from p-type to n-type at about 45% mole fraction InSb concentration in the solid [36]. Generating current-induced Peltier heating or cooling at the melt-solid interface in the InSb-GaSb system depends on the electronic behavior of the system. Due to rejection of InSb at the interface, the growing ingot contains less InSb initially and more near the end. It means that the materials changes from p-type to n-type somewhere along the ingot. If continuous Peltier cooling pulses are needed to demarcate the interface, the direction of current must be switched from one polarity to another when the ingot changes from p-type to n-type. Te-doping also changes the electronic behavior of the InSb-GaSb system.

In this work, we tried to determine the dependence of Peltier effect on the current polarity in GaSb system. Also we tried to measure the thermal perturbations induced in the melt and in the vicinity of the liquid-solid interface in GaSb. These results were used to separate the effects of Joule heating, Thomson heating and cooling, and Peltier heating and cooling in GaSb.

In this section we report results of *in-situ* temperature measurements in melts of $In_xGa_{1-x}Sb$ and in GaSb during passage of electric current pulses. The temperature measurement technique is given in Chapter 3. In brief, an ungrounded K-type sheathed thermocouple was placed in a charge of in a vacuum sealed ampoule. The charge was

contacted on top and bottom by two molybdenum-graphite electrodes used for passage of electrical current. The available programmable current generator could supply up to 10 amp current. Current amplitudes of 2 to 10 amp were tried. Here we report the temperature measurements for 10 amp current. The thermocouple was connected to a thermocouple board of a data acquisition system and a Zenith 248 computer. Pulse durations of 5, 30, and 60 sec were used in these experiments.

Overall, seven individual ampoules were prepared for temperature measurements. Only three experiments were successful. The other four were terminated due to failure of the thermocouple sheath or by leakage of melt from the bottom electrode, resulting in loss of electrical contact between the electrodes and charge.

Temperature Measurements in Molten $In_{0.2}Ga_{0.8}Sb$

Several temperature measurements were performed in a molten charge of prealloyed $In_{0.2}Ga_{0.8}Sb$. The charge was 7 cm long and situated in a quartz ampoule of 9 mm inner diameter and 11 mm outer diameter. An ungrounded K-type thermocouple with 0.41 mm diameter 304 stainless steel sheath was placed 3.5 cm into the charge from bottom. In these measurements a strip-chart recorder and digital thermometer were used to record and monitor the thermocouple readings in the charge. The entire charge was situated in the heater section of the furnace. The heater and cooler settings were 820°C and 450°C, respectively. After melting the charge, the thermocouple reading in the charge was allowed to reach steady-state before application of current.

Figure 4.61 shows the thermocouple readings in the melt of $In_{0.2}Ga_{0.8}Sb$ during periodic passage of 10 amp current for 60 sec followed by no current for 30 off. The thermocouple reading was initially at 815.7°C before application of current. The temperature periodically varied between 815.7°C to 817.2°C. The temperature in the melt increased gradually during current passage and decayed when it was off.

Figure 4.62 shows thermocouple readings in the $In_{0.2}Ga_{0.8}Sb$ melt during periodic passage of 10 amp alternating current pulses for 30 s with positive polarity and 30 with negative polarity. The thermocouple reading was initially at 808.9°C before application of

current. The temperature of the melt increased due to a new steady state of about 811.5°C. The temperature remained fairly constant during alternating current pulses. Due to the low resolution of the strip-chart recorder, the periodic Thomson cooling and heating were not detectable.

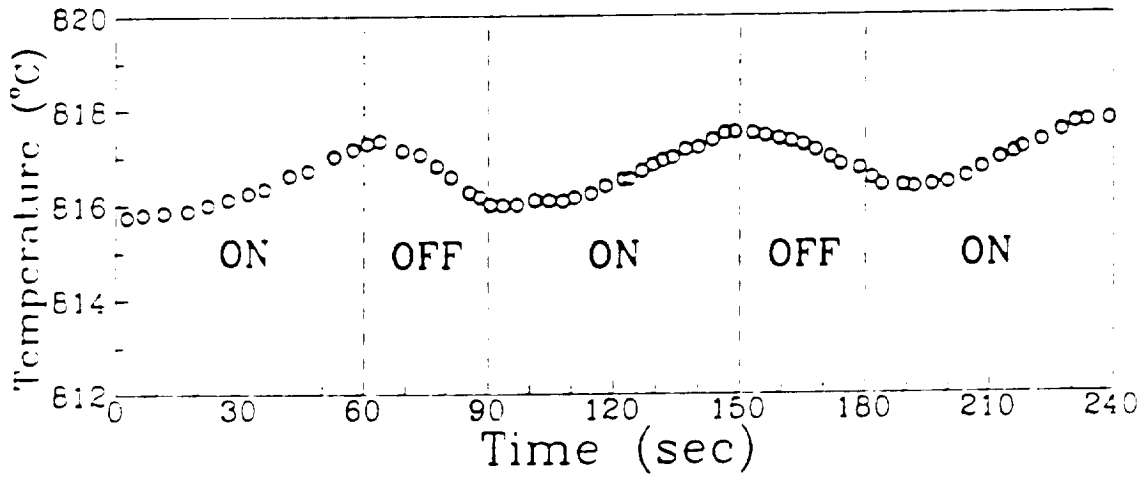

Figure 4.61: Thermocouple readings in molten $In_{0.2}Ga_{0.8}Sb$ during passage of 10 amp current for 60 sec followed by no current for 30 sec. The current was passed from the top electrode to the bottom electrode. The tip of the thermocouple was situated 3.5 cm into the 7 cm long charge.

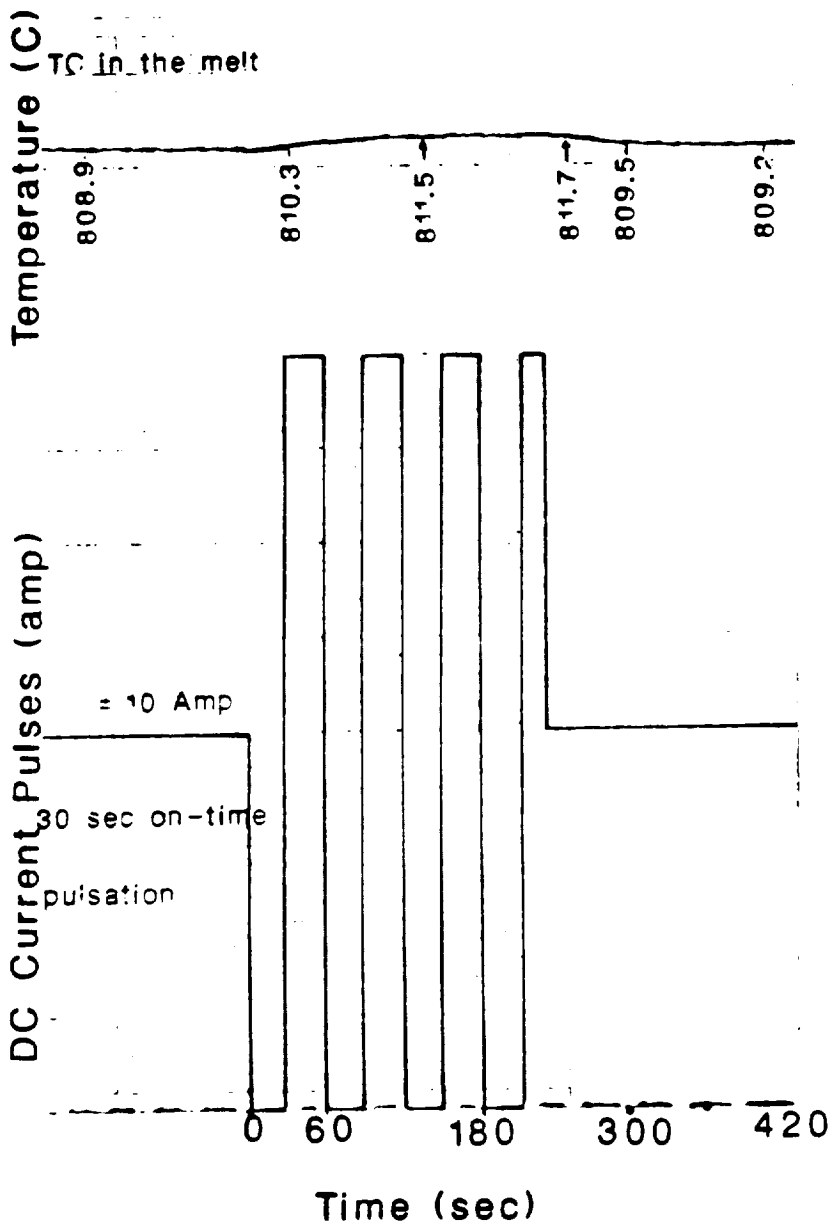

Figure 4.62: Thermocouple readings in molten $In_{0.2}Ga_{0.8}Sb$ during passage of 10 amp current alternating for 30 sec (+) followed by 30 sec (-). The tip of the thermocouple was situated 3.5 cm into the 7 cm long charge.

Temperature Measurements in GaSb

Several *in-situ* temperature measurements were performed in GaSb during passage of current. The objective of these experiments was to measure the current-induced thermal perturbations in GaSb due to Joule heating, Thomson heating or cooling and Peltier effect. GaSb was used instead of $In_{0.2}Ga_{0.8}Sb$. The freezing temperature of InSb-GaSb varies along the ingot. It was difficult to determine the exact position of the thermocouple tip with respect to the freezing temperature of the InSb-GaSb charge. By knowing the freezing temperature of GaSb, it was possible to position the tip of thermocouple junction in the vicinity of the interface. These measurements were performed using a K-type thermocouple with stainless steel sheath placed in a charge of GaSb. The tip of the thermocouple was positioned 3.5 cm into a 7 cm long GaSb charge. The success of these experiments was limited by the failure of the thermocouple in the melt. The melt soon damaged the sheath and the thermocouple junction. These measurements were performed with heater and cooler settings of 800°C and 475°C, respectively, a 5 cm insulation layer, and a stationary ampoule.

Figure 4.63 shows the thermocouple readings in the GaSb melt during passage of 10 amp current alternating for 30 sec (+) polarity and 30 sec (-) polarity. In recording T1, the molten charge was situated in the middle of the heater. Recording T2 was made after the ampoule containing the charge and thermocouple was moved 1.5 cm down from where recording T1 had been taken. The axial temperature gradient was higher at the position where T2 was taken than where T1 was taken. In T1, the passage of current was initiated after 20 sec. The thermocouple reading showed a temperature rise from 780.5°C to 782.2°C, and then the thermocouple reading remained at about 782°C throughout the remaining of pulsations, indicating a new near-equilibrium was established. Small temperature fluctuations were observed during the change of direction of current due to the contribution of the Thomson effect.

In T2 the temperature increased from 774°C to 776.8° and afterward varied periodically by 0.7°C during positive and negative alternating current.

In both T1 and T2, the temperature rise was due to Thomson heating and Joule heating. The periodic temperature rise and fall were due to the contribution of Thom-

son heating and cooling as the direction of current was changed. The periodic Thomson heating and cooling was less pronounced in T1 as compared to T2. Such a difference was probably due to the higher temperature gradient in the molten charge where the profile T2 was recorded as compared to the T1. The presence of liquid-solid interface was unlikely in these measurements. If any solid phase was present, the liquid-solid interface would have been about 3 cm away from thermocouple tip in recording T2. Peltier cooling possibly had some effect on these thermal perturbations.

The Thomson effect is a reversible phenomenon depending on the direction of current. The Thomson heat is expressed as:

$$Q_t = \tau I \frac{dT}{dX} \tag{4.22}$$

where $\frac{dT}{dX}$ is the temperature gradient. I is the current density , and τ is the Thomson coefficient. Joule heating is expressed as:

$$Q_j = \rho I^2 \tag{4.23}$$

where ρ is the electrical resistivity and I is the current density. Joule heating is independent of the direction of applied current.

A single pulse measurement was performed at the same position where profile T2 was taken. Figure 4.64 shows the thermocouple reading in the GaSb melt during passage of 10 amp current. The pulse was passed for 60 sec from the top electrode (-) to bottom electrode (+), and then vice versa. The thermocouple readings when the pulse was passed from top electrode (-) to bottom electrode (+) showed a 0.6°C temperature difference due to Thomson effect by passing different polarity current. In these measurements, the temperature rise in the melt was due to Joule heating and Thomson heating when the current was passed from top(-) to bottom(+). The reversed polarity resulted in Joule heating and Thomson cooling in the melt. In these measurements, the presence of liquid-solid interface was unlikely.

Table 4.8 shows the power per unit volume generated in a GaSb melt for 15.7 amp/cm^2 current density due to Joule heating and Thomson effect. Two temperature

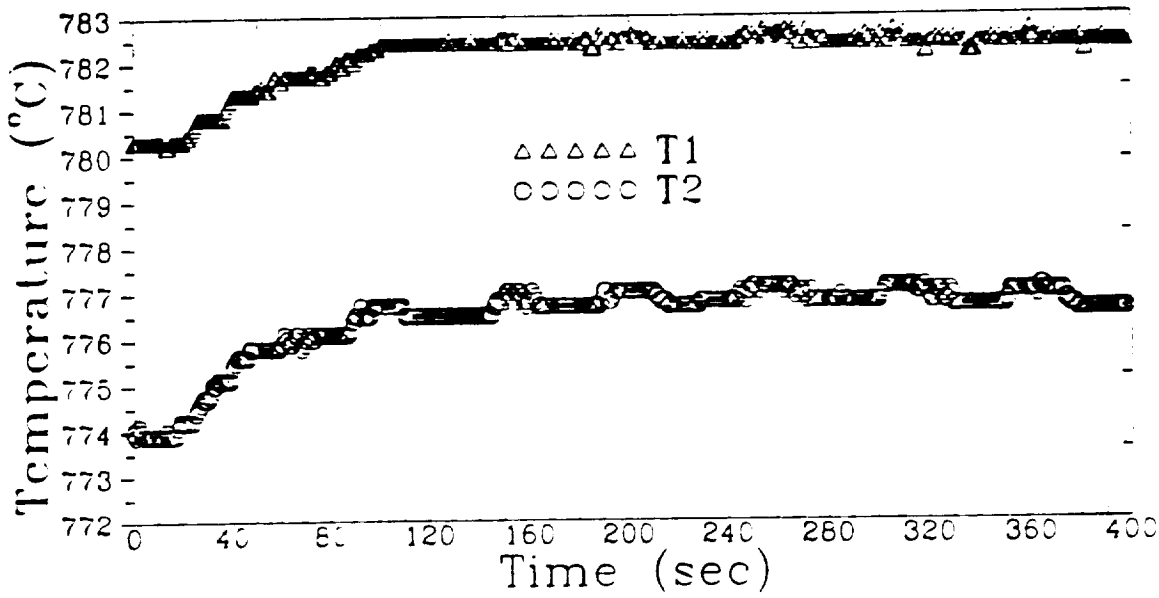

Figure 4.63: Thermocouple readings in the GaSb melt during passage of 10 amp current alternating for 30 sec (+) polarity and 30 sec (-) polarity. The Passage of current was initiated after 20 sec on the time scale. Recording T1 and T2 were taken at positions with low and high axial temperature gradients, respectively. The temperature increase was due to Joule heating and Thomson effects. Larger periodic thermal perturbations were measured T2 as compared to T1 due to the periodic contribution of Thomson heating and cooling because of larger temperature gradient in T2.

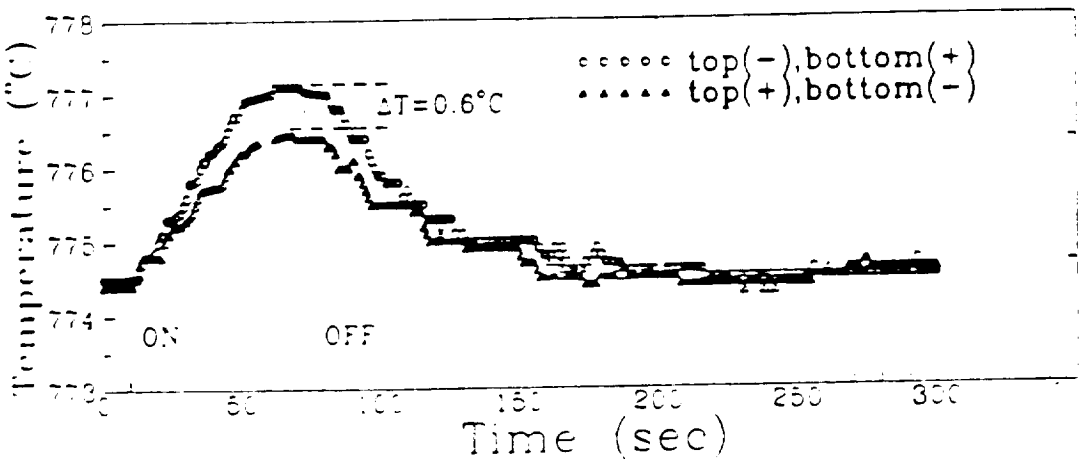

Figure 4.64: Thermocouple readings in a GaSb melt during passage of 10 amp current for 60 sec passed from top electrode(-) to bottom electrode(+), and the vice versa. The thermocouple tip was in the same position as T2 in Figure 4.63. The temperature increase was due to Joule heating and Thomson effects. The temperature difference of 0.6 °C was due to contribution of Thomson heating or cooling.

gradients were used in these calculations; 2°C/cm for low temperature gradient region in the melt, such that in the middle of the heater, and 20°C/cm a for high temperature gradient region, as in the vicinity of the liquid-solid interface. For 10 amp current, the power generated by Joule heat is about 10 times larger than the Thomson power in a 2°C/cm axial temperature gradient.

Table 4.8: Power generated in the melt of GaSb due to 15.7 amp/cm^2 current density.

Current Density amp/cm^2	Joule watt/cm^3	Thomson watt/cm^3	
		2°C/cm	20°C/cm
±15.7	0.023	±.00157	±0.0157

To measure the thermal perturbations in the vicinity of the liquid-solid interface, the ampoule was translated into the cooler to promote solidification. The thermocouple reading was monitored, meanwhile. When the thermocouple reading reached 720°C the translation was terminated.

This temperature reading was 2-5° above the melting temperature of GaSb, i.e. 715°C to 718°C.. With an axial temperature gradient of 20-25°C/cm in the vicinity of interface, the thermocouple tip at 720°C temperature reading was expected to be 2 to 3 mm away from interface into the melt.

The temperature was measured during application of 10 amp current passed for 60 sec from melt to solid and vice versa. Figure 4.65 shows the thermocouple readings in the vicinity of the liquid-solid interface, 2 to 3 mm into the melt of GaSb. A 10 amp current was passed for 60 sec from melt (+) to solid (-) for 60 sec. Initially, the thermocouple reading decreased from 720°C to 714°C within the first 5-6 sec of pulsation. Afterward, the temperature started increasing gradually. When the pulse was turned off, the cooling

effect of the current was terminated and the thermocouple reading started rising to the temperature reading before pulsation. A slight overshoot was observed after the current was turned off. This could have been due to volumetric Joule heating which had not dissipated completely, even after termination of the current. The initial cooling behavior was due to Peltier and Thomson cooling. Although the cooling effect remained throughout the pulse. Joule heating resulted in a gradual rise of temperature.

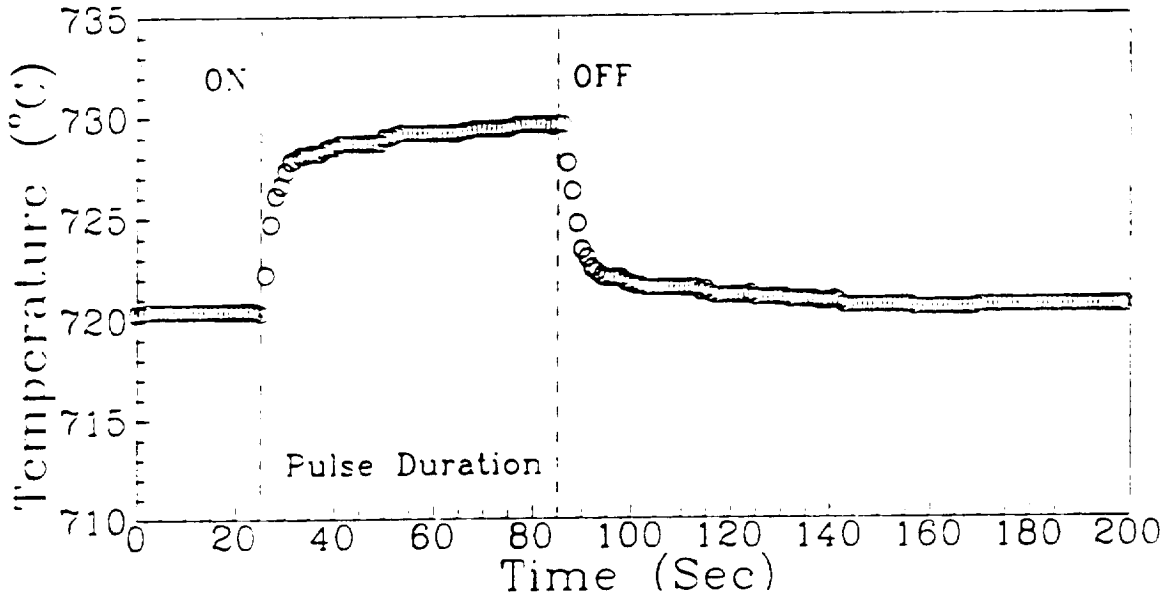

Figure 4.65: Thermocouple readings in a GaSb melt in the vicinity of the liquid-solid interface during passage of 10 amp current for 60 sec passed from solid, i.e. bottom electrode(+) to melt, i.e. top electrode(-). Before current pulsation, the thermocouple tip was estimated to have been 2 to 3 mm away from the interface in the melt. The temperature rise was dominated by Peltier heating initially and followed by Joule heating and Thomson heating. After termination of current the thermocouple reading returned to the initial steady-state value.

Figure 4.66 shows the thermocouple reading in the melt of GaSb in the vicinity

of the liquid-solid interface for a 10 amp current pulse passed for 60 sec from solid(+) to melt (-). These temperature measurements were performed at the same position as the profile given in the Figure 4.66, except with different polarity. Initially, the temperature started rising rapidly, mostly due to Peltier heating, from 720°C to 726°C within the first 6-8 sec of current pulsation and then continued increasing up to 728.5°C. After termination of current, the temperature decayed to its initial value.

Figure 4.67 shows temperature measurements similar to those in Figures 4.65 and 4.66, except the pulse duration was 5 sec. Similar temperature decay and rise was observed as in Figures 4.65 and 4.66 during the first 5 sec of the pulsation.

In these measurements, the transient thermal perturbations in the vicinity of the interface was dominated by the Peltier effect and possibly the Thomson effect. Joule heating was less pronounced initially. As the current pulsation was continued, the interface would have moved to a new position and the Joule heating-induced thermal rise became more pronounced.

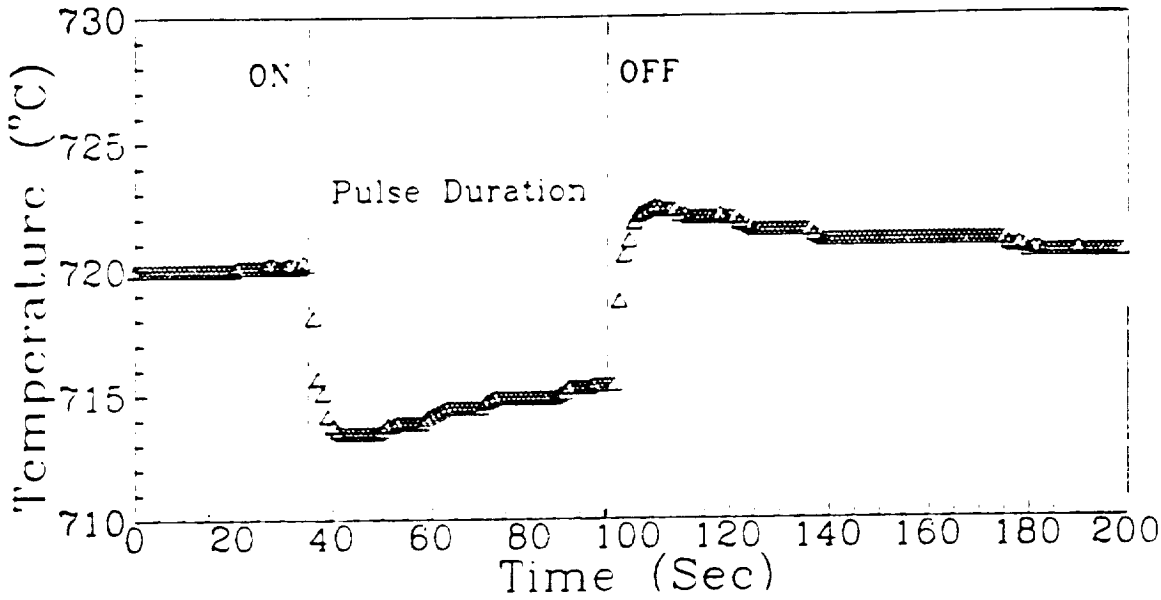

Figure 4.66: Thermocouple readings in a GaSb melt in the vicinity of the liquid-solid interface during passage of 10 amp current for 60 sec passed from solid, i.e. bottom electrode(-) to melt, i.e. top electrode(+). Before current pulsation, the thermocouple tip was estimated to have been 2 to 3 mm away from interface in the melt. The temperature decay was dominated by Peltier cooling initially, followed a slight increase due to Joule heating and relocation of the interface position. After termination of the current the thermocouple reading returned to the initial steady-state value.

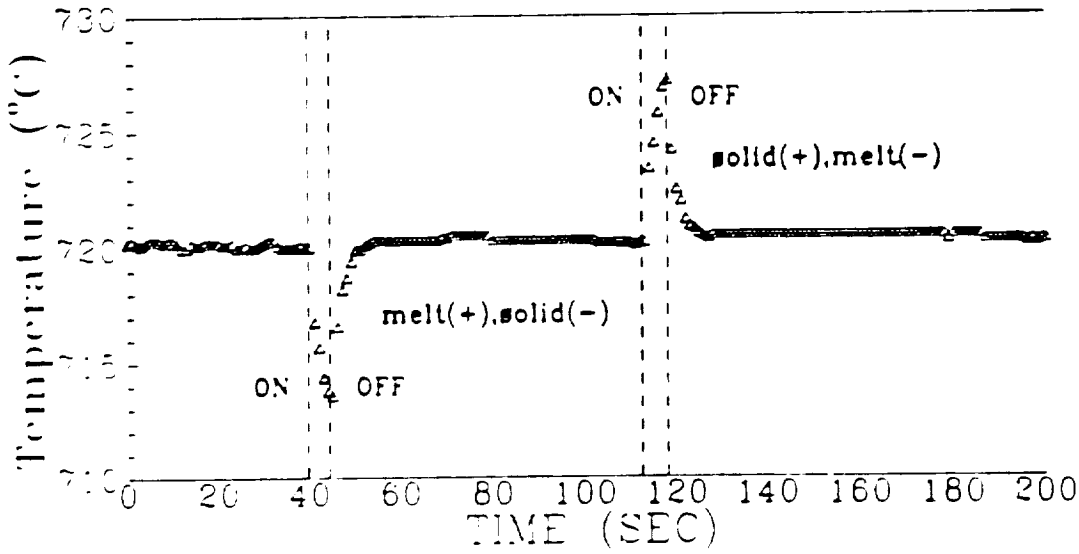

Figure 4.67: Thermocouple readings in the melt of GaSb charge in the vicinity of liquid-solid interface during passage of 10 amp current for 5 sec passed from solid, i.e. bottom electrode(+) to melt, i.e. top electrode(-) and vice versa. Before pulsation, the thermocouple tip was possibly 2 to 3 mm away from interface into the melt. The temperature rise and fall for different polarities were mostly due to Peltier effect. After termination of current the thermocouple reading returned to the initial steady-state value.